RMetS
Royal Meteorological Society

Role of large eddies in the breakdown of the Reynolds analogy in an idealized mildly unstable atmospheric surface layer

Kaighin A. McColl,[a,b]* Chiel C. van Heerwaarden,[c] Gabriel G. Katul,[d,e] Pierre Gentine[f] and Dara Entekhabi[a,g]

[a]*Department of Civil and Environmental Engineering, MIT, Cambridge, MA, USA*
[b]*Department of Earth and Planetary Sciences, Harvard University, Cambridge, MA, USA*
[c]*Meteorology and Air Quality Section, Wageningen University, The Netherlands*
[d]*Nicholas School of the Environment, Duke University, Durham, NC, USA*
[e]*Department of Civil and Environmental Engineering, Duke University, Durham, NC, USA*
[f]*Department of Earth and Environmental Engineering, Columbia University, New York, NY, USA*
[g]*Department of Earth, Atmospheric and Planetary Sciences, MIT, Cambridge, MA, USA*

*Correspondence to: K. A. McColl, MIT Building 48-216, 77 Massachusetts Avenue, Cambridge, MA 02139, USA.
E-mail: kmccoll@mit.edu

While the breakdown in similarity between turbulent transport of heat and momentum (or Reynolds analogy) is not disputed in the atmospheric surface layer (ASL) under unstably stratified conditions, the causes of this breakdown are still debated. One reason for the breakdown is differences between how coherent structures transport heat and momentum, and their differing responses to increasing instability. Monin – Obukhov Similarity Theory (MOST), which hypothesizes that only local length-scales play a role in ASL turbulent transport, implicitly assumes that large-scale structures are inactive, despite their large energy content. Widely adopted mixing-length models also rest on this assumption in the ASL. The difficulty of characterizing low-wavenumber turbulent motions with field measurements motivates the use of high-resolution Direct Numerical Simulation (DNS), which is free from subgrid-scale parametrizations and *ad hoc* assumptions near the boundary. Despite the low Reynolds number and idealized geometry of the DNS, DNS-estimated MOST functions are consistent with ASL field experiments, as are low-frequency features of the spectra. Parsimonious spectral models for MO stability correction functions for momentum (ϕ_m) and heat (ϕ_h) are derived, based on idealized vertical velocity variance and buoyancy variance spectra fit to the corresponding DNS spectra. For ϕ_m, a spectral model, based only on local length-scales, matches DNS and field measurements well. In contrast, for ϕ_h, the model is substantially biased unless contributions from larger length-scales are also included. These results are supported by sensitivity analyses based on field measurements that are independent of the DNS. They show that ASL heat transport is not MO-similar, even under mild stratification, and in the absence of entrainment, non-stationarity and canopy effects. It further suggests that the breakdown of the Reynolds analogy is at least partially caused by the influence of large eddies on turbulent heat transport.

Key Words: coherent structures; Direct Numerical Simulation; Monin – Obukhov Similarity Theory; mixing length; Reynolds analogy; transport efficiencies; turbulent spectra

Received 11 October 2016; Revised 15 May 2017; Accepted 17 May 2017; Published online in Wiley Online Library

1. Introduction

Turbulent transport processes dominate the exchange of heat, momentum and scalars between the Earth's surface and its lower atmosphere. During the day, surface turbulence is often both shear- and buoyancy-generated, greatly complicating the modelling of these exchanges. Monin – Obukhov Similarity Theory (MOST) has been the dominant theory for describing these exchanges in the atmospheric surface layer (ASL). First introduced six decades ago, MOST has made it possible to measure and model turbulent fluxes in the ASL, which is typically characterized by very high Reynolds numbers. MOST assumes the flow statistics are governed by four parameters, which can all be measured in the lower atmosphere (Monin and Obukhov,

1954). Given this assumption, it uses dimensional analysis to relate normalized flow statistics to a single, non-dimensional stability parameter, ζ. Distortions of the mean velocity and buoyancy profiles, due to thermal stratification, are also related solely to ζ ($\phi_m(\zeta)$ and $\phi_h(\zeta)$, respectively). These functions can be interpreted as adjustments to the near-neutral turbulent eddy diffusivities of momentum and heat, respectively. The exact functional forms relating the flow statistics and eddy diffusivities to ζ are not prescribed by MOST. They have been typically obtained from field experiments, and often display significant scatter (e.g. Businger *et al.*, 1971). Yet, despite their limitations, these functions are widely used to parametrize surface layer turbulence in weather and climate models, with implications for modelled boundary-layer dynamics (Brasseur and Wei, 2010; Shin and Hong, 2011; Bosveld *et al.*, 2014).

It is commonly assumed that the turbulent transport of heat and momentum are similar (the so-called 'Reynolds analogy', where $\phi_m = \phi_h$). While ϕ_m and ϕ_h are comparable for mildly stable and near-neutral conditions, they differ under unstable conditions (Kaimal and Finnigan, 1994). The breakdown of the Reynolds analogy implies differences in the mechanisms governing the turbulent transport of heat and momentum. Turbulent coherent structures, and their dependence on stratification, may be one plausible mechanism explaining this difference (de Bruin *et al.*, 1993; Choi *et al.*, 2004; Li and Bou-Zeid, 2011). In the absence of heating, the characteristic coherent structure in wall-bounded turbulent flows is the hairpin vortex (e.g. Head and Bandyopadhyay, 1981; Perry and Chong, 1982; Adrian, 2007). These structures are mainly confined to the near-wall region, although they can sometimes extend across the full boundary-layer height. In the presence of heating, the hairpin vortices increase their inclination angle away from the wall (Hommema and Adrian, 2003), before ultimately forming vertical thermal plumes, spanning the full boundary-layer height (Kaimal and Finnigan, 1994).

The fundamentally different vertical length-scales of these two types of coherent structures is not accommodated by many models of atmospheric turbulence. For instance, a commonly used model for the ASL requires that all turbulent length-scales must be proportional to a master length-scale l_m, often specified to be proportional to the height above the surface (Mellor, 1973; Mellor and Yamada, 1982), with empirical adjustments to allow variations with stability conditions (Therry and Lacarrere, 1983; Nakanishi, 2001). Even with considerable tuning of parameters, this class of models struggles to reproduce the observed dissimilarity between ϕ_m and ϕ_h in unstable conditions (Nakanishi, 2001). Therefore, a model based on a single length-scale seems insufficient. Yet, for computational tractability, it is clearly essential to limit the number of modelled length-scales.

A natural framework for parsimoniously modelling multiple length-scales is by modelling the spectra of turbulent fluctuations. The shape and magnitude of the spectra are constrained by theory and observations. The most well-established constraint is from Kolmogorov's scaling in the so-called inertial range, encompassing turbulent motions much larger than viscous dissipation scales, but much smaller than the flow's integral length-scale (Kolmogorov, 1941). This scaling has been exploited in a range of studies seeking to explain the shapes of ϕ_m (Katul *et al.*, 2011; Li *et al.*, 2012, 2016a; Salesky *et al.*, 2013), ϕ_h (Katul *et al.*, 2013) and related quantities, such as the turbulent Prandtl number (Katul *et al.*, 2014; Li *et al.*, 2015a, 2015b) and turbulent Schmidt number (Katul *et al.*, 2016). However, while Kolmogorov scaling is well-established in the inertial range, the scaling of larger eddy length-scales (outside the inertial range) is more uncertain. These scales have been modelled simply in all previous studies, usually qualitatively based on limited observations from field experiments. However, field experiment spectra are particularly susceptible to estimation errors at low wavenumbers, and are usually substantially filtered in this range (Kaimal *et al.*, 1972; Högström *et al.*, 2002). Hence, there is still considerable uncertainty about the role of large eddies in determining ϕ_m and ϕ_h (Katul *et al.*, 2013).

The weaknesses of field observations for characterizing low-wavenumber turbulent motions motivates the use of high-resolution simulations. Khanna and Brasseur (1997) were the first to use large-eddy simulation (LES) to test the validity of MOST. However, the choice of a subgrid-scale (SGS) filter used in LES has a significant, and uncertain, impact on LES outputs in the near-wall region, precisely where MOST applies (Brasseur and Wei, 2010). In contrast to LES, DNS resolves all scales of the flow, avoiding the need for SGS filters and *ad hoc* stitching between the wall and the fluid, but at the price of much greater computational burden and reduced inertial subrange. Since the computational cost scales with Reynolds number, DNS is only viable for turbulent simulations of low-to-moderate Reynolds number flows. (Sullivan and Patton, 2011, show that LES also implicitly introduces an effective Reynolds number that is restricted to low-to-moderate values). By 'low-to-moderate Reynolds numbers', we refer to flows where the Reynolds number is sufficiently large to generate eddies across a broad range of sizes, but the separation between scales where turbulence is produced and dissipated is not as extensive as in the ASL. Perhaps for this reason, prior studies that used DNS to test MOST scaling in an (idealized) mildly unstable ASL are rare or perhaps absent altogether. As shown here, despite the low Reynolds number and highly idealized conditions, DNS estimates of MOST similarity functions for mildly unstable conditions are largely consistent with field experiments, suggesting DNS may provide useful insights into the role of large eddies in determining the shapes of ϕ_m and ϕ_h.

The objective of this work is to diagnose the role of large-eddy contributions to differences between ϕ_m and ϕ_h in mildly unstable conditions, using a DNS of a highly idealized ASL. The paper is organized as follows. In section 2, idealized models of ϕ_m and ϕ_h are introduced, based on parametrizations of the spectra of turbulent vertical velocity variance and buoyancy. In section 3, we describe the DNS used in this study, and compare it with field experiment measurements. Results are presented and discussed in sections 4 and 5, respectively.

2. Theory

In this section, we review MOST, and derive spectral models for the MOST stability functions ϕ_m and ϕ_h. Throughout, x, y and z refer to the streamwise, lateral and vertical directions, respectively; and u, v and w refer to the streamwise, lateral and vertical velocities. The buoyancy is defined as $b = \beta(T - T_0)$, where T is temperature, $\beta = g/T_0$ is the buoyancy parameter under the Boussinesq approximation, g is gravitational acceleration, and T_0 is a reference temperature. Buoyancy is adopted as the state variable rather than T or potential temperature θ in this study. Furthermore, the effects of water vapour on air density are ignored (i.e. we consider a dry ASL). The variables u, v, w and b are decomposed into Reynolds-averaged mean states (e.g. for streamwise velocity, denoted U) and turbulent excursions (e.g. u') such that $u = U + u'$, with similar notation used for the other variables.

2.1. Monin – Obukhov similarity theory

We first review the assumptions and terminology of MOST. The ASL begins at a height sufficiently high above the land surface as to be unaffected by surface roughness elements, and extends to a height of approximately 50 – 100 m into the atmosphere, such that it is still unaffected by the Coriolis force (e.g. Brutsaert, 1982; Kaimal and Finnigan, 1994). In this layer, MOST predicts the turbulent flow is governed by four parameters: the height above ground or zero-plane displacement z, the buoyancy parameter β, the friction velocity $u_*^2 = \tau/\rho$ and the 'surface' kinematic heat flux $q/(\rho c_p)$ (Monin and Obukhov, 1954). Here, τ/ρ is the

'surface' shear stress, ρ is the fluid density, q is the surface sensible heat flux, and c_p is the fluid's specific heat capacity at constant pressure. 'Surface' stresses and fluxes are in fact typically estimated several metres above the land surface using eddy covariance measurements (Högström, 1988; Kaimal and Finnigan, 1994). These four parameters are used to define a velocity scale (u_*), buoyancy scale ($b_* = \beta q/(\rho c_p u_*)$), and length-scale

$$L = \frac{-u_*^3}{k_v \beta \frac{q}{\rho c_p}}, \tag{1}$$

where k_v is von Kármán's constant (a value of 0.41 is used in this study, consistent with the bulk of experiments). MOST assumes that turbulent diffusion dominates molecular diffusion, that the flow is stationary and planar-homogeneous, that subsidence is negligible and that there is no horizontal pressure gradient (Brutsaert, 1982). Under these conditions, the momentum and energy budgets reduce to

$$\overline{u'w'} = -u_*^2 \tag{2}$$

and

$$\overline{w'b'} = u_* b_*, \tag{3}$$

respectively. The scales u_*, b_* and L can be used in dimensional analysis to relate non-dimensionalized properties of ASL turbulence to universal similarity functions of $\zeta = z/L$; in particular, the non-dimensionalized vertical velocity standard deviation,

$$\phi_w = \frac{\sigma_w}{u_*}, \tag{4}$$

non-dimensionalized buoyancy standard deviation,

$$\phi_b = \frac{\sigma_b}{b_*}, \tag{5}$$

non-dimensionalized mean velocity gradient,

$$\phi_m = \frac{k_v u_* z}{-\overline{u'w'}} \frac{\mathrm{d}U}{\mathrm{d}z}, \tag{6}$$

and non-dimensionalized mean buoyancy gradient,

$$\phi_h = \frac{k_v u_* z}{\overline{w'b'}} \frac{\mathrm{d}B}{\mathrm{d}z}, \tag{7}$$

where σ_w^2 and σ_b^2 are the vertical velocity variance and buoyancy variance, respectively. Note that ϕ_m and ϕ_h are related to the turbulent eddy diffusivities of momentum (K_m) and heat (K_h), and their corresponding 'mixing lengths' (l_m and l_h, respectively) by the following:

$$-\overline{u'w'} = \frac{k_v u_* z}{\phi_m} \frac{\mathrm{d}U}{\mathrm{d}z} = l_m u_* \frac{\mathrm{d}U}{\mathrm{d}z} = -K_m \frac{\mathrm{d}U}{\mathrm{d}z}, \tag{8}$$

$$\overline{w'b'} = \frac{k_v u_* z}{\phi_h} \frac{\mathrm{d}B}{\mathrm{d}z} = l_h u_* \frac{\mathrm{d}B}{\mathrm{d}z} = -K_h \frac{\mathrm{d}B}{\mathrm{d}z}. \tag{9}$$

The functions relating ϕ_m and ϕ_h to ζ cannot be specified by MOST and have typically been estimated from field experiments (e.g. Businger *et al.*, 1971).

2.2. TKE and buoyancy variance budgets

The MOST variables ϕ_w and ϕ_b may be viewed as dimensionless measures of the turbulent vertical kinetic energy and turbulent potential energy, respectively. We aim to relate these quantities to the MOST variables linked to turbulent transport of momentum (ϕ_m) and heat (ϕ_h). This requires the introduction of the turbulent kinetic energy (TKE) budget, which is assumed to be at steady state,

$$\epsilon = -\overline{u'w'} \frac{\mathrm{d}U}{\mathrm{d}z} + \overline{w'b'}, \tag{10}$$

where ϵ is the mean TKE dissipation rate, and we assume production and dissipation terms dominate in the TKE budget, a reasonable assumption in the constant flux layer that is tested later on. This equation can be rewritten in terms of MOST similarity variables as

$$\epsilon = \frac{\left(-\overline{u'w'}\right)^2}{k_v u_* z} \left(\phi_m\left(\frac{z}{L}\right) - \frac{z}{L}\right). \tag{11}$$

The steady state buoyancy variance budget can be simplified to

$$N_b = \overline{w'b'} \frac{\mathrm{d}B}{\mathrm{d}z}, \tag{12}$$

where N_b is the buoyancy variance dissipation rate, and we assume production and dissipation terms dominate the buoyancy variance budget, as for the TKE budget (this assumption is also tested later). There are different definitions of N_b in the literature; we define N_b as the rate of destruction of half the buoyancy variance, consistent with other references (Kaimal *et al.*, 1972; Stull, 1988). This relation can be written as

$$N_b = \frac{b_*^2 u_*}{k_v z} \phi_h. \tag{13}$$

2.3. Mixing-length models for ϕ_m and ϕ_h

To finalize model development, relations linking the dissipation rates ϵ and N_b to ϕ_w and ϕ_b are required. In this section, these relations are obtained from the assumed vertical velocity variance spectra $F_{ww}(k, z)$ and the buoyancy variance spectra $F_{bb}(k, z)$, where k is the wavenumber in the longitudinal direction. We show how these relations link to a common class of models in the literature: 'mixing-length' models.

Consider an idealized two-regime spectrum for F_{ww} (Figure 1(a)) considered in previous studies (e.g. Katul *et al.*, 2013; Li *et al.*, 2015b):

$$F_{ww}(k) = \begin{cases} C_K \epsilon^{2/3} k^{-5/3} & \text{for } k \geq k_{aw}, \\ C_K \epsilon^{2/3} k_{aw}^{-5/3} & \text{for } k < k_{aw}, \end{cases} \tag{14}$$

where C_K is the Kolmogorov constant for the vertical velocity (≈ 0.65 from high Reynolds number experiments), and k_{aw} is a transition wavenumber. Integrating this assumed spectrum between $k = 0$ and $k = \infty$ yields $\sigma_w^2 = (5/2) C_K \epsilon^{2/3} k_{aw}^{-2/3}$. If we define $k_{aw} = 2\pi/l_w$, then rearranging gives

$$\epsilon = \left(\frac{2}{5C_K}\right)^{3/2} \frac{2\pi\sigma_w^3}{l_w} \propto \frac{\sigma_w^3}{l_w}. \tag{15}$$

Here, $2\pi/l_w$ is the wavenumber corresponding to the peak of the compensated spectrum kF_{ww} (Figure 1(c)). Combining Eqs (11) and (15) gives

$$\phi_m\left(\frac{z}{L}\right) = \frac{z}{L} + \frac{2^{5/2}\pi}{(5C_K)^{3/2}} \left(\frac{k_v z}{l_w}\right) \phi_w^3. \tag{16}$$

This model is dependent on the specification of l_w, a length-scale corresponding to the breakpoint in the F_{ww} spectrum and the peak of the compensated spectrum kF_{ww} (Figure 1). Experimental measurements demonstrate that this length-scale is proportional to the mixing-length l_m derived from the wind speed profile across a broad range of atmospheric stability conditions (Pena *et al.*, 2010). A common specification in the ASL is

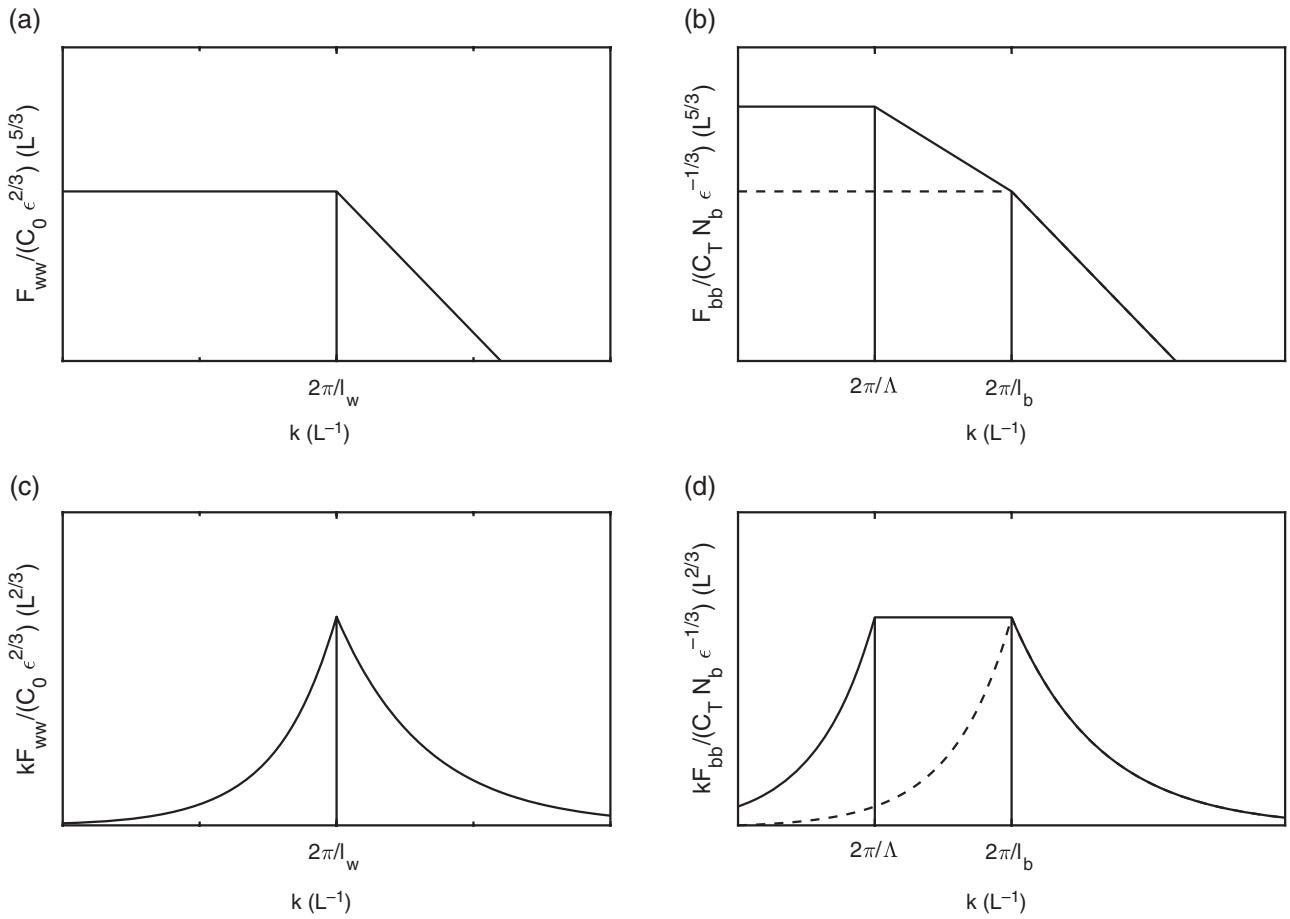

Figure 1. Idealized forms used for F_{ww} and F_{bb}. (a) Idealized F_{ww} given in Eq. (14), with logarithmic x- and y-axes. (b) Idealized F_{bb} given in Eq. (17) (dashed line) and Eq. (20) (solid line), with logarithmic x- and y-axes. (c) Compensated idealized vertical velocity variance spectrum, with logarithmic x-axis and linear y-axis, highlighting that the spectrum peaks at $k = 2\pi/l_w$. (d) Compensated idealized buoyancy variance spectrum, with logarithmic x-axis and linear y-axis. Without a k^{-1} region (dashed line), the compensated spectrum exhibits a distinct peak at $k = 2\pi/l_b$. When a k^{-1} region is included (solid line), the spectrum does not have a distinct peak.

simply $l_m = k_v z$ (e.g. Mellor, 1973; Mellor and Yamada, 1982), consistent with Prandtl's 'mixing length' hypothesis (Prandtl, 1925), and Townsend's 'attached eddy' hypothesis (Townsend, 1980). Various empirical corrections (e.g. Therry and Lacarrere, 1983; Nakanishi, 2001; Zilitinkevich *et al.*, 2006) have been proposed to this model to include dependence of l_m on stability ($\zeta = z/L$). Because l_m and l_w are proportional to each other, we refer to Eq. (16) as a 'mixing-length' model for ϕ_m. One advantage of working with l_w rather than l_m is that l_w can be independently estimated from measured F_{ww}. Furthermore, as we will show in section 2.4, a spectral model (and corresponding spectral parameters such as l_w) can be easily generalized to instances where more than one length-scale contributes significantly to the flow variance.

A mixing-length model for ϕ_h could be derived in a similar fashion to that for ϕ_m. Consider an idealized two-regime spectrum for the buoyancy variance $F_{bb}(k)$ (Figure 1(b), dashed line):

$$F_{bb}(k) = \begin{cases} C_T N_b \epsilon^{-1/3} k^{-5/3} & \text{for } k \geq k_{ab}, \\ C_T N_b \epsilon^{-1/3} k_{ab}^{-5/3} & \text{for } k < k_{ab}, \end{cases} \tag{17}$$

where $C_T \approx 0.8$ is the Kolmogorov–Obukhov–Corrsin constant, and k_{ab} is a transition wavenumber, analogous to k_{aw} in the vertical velocity variance spectrum. Integrating this between $k = 0$ and $k = \infty$ gives $\sigma_b^2 = (5/2) C_T N_b \epsilon^{-1/3} k_{ab}^{-2/3}$. If we define $k_{ab} = 2\pi/l_b$, then

$$N_b = \frac{2^{5/3}\pi^{2/3}}{5C_T} \frac{\sigma_b^2 \epsilon^{1/3}}{l_b^{2/3}} \propto \frac{\sigma_b^2 \epsilon^{1/3}}{l_b^{2/3}}. \tag{18}$$

Again, l_b corresponds to the transition length-scale $2\pi/k_{ab}$. Alternatively, $2\pi/l_b$ is the wavenumber corresponding to the peak of the compensated spectrum $kF_{bb}(k)$ (Figure 1(d), dashed line). Combining Eqs (18), (15) and (13) gives

$$\phi_h\left(\frac{z}{L}\right) = \left(\frac{2^{5/2}\pi}{5^{3/2} C_T C_K^{1/2}}\right)\left(\frac{k_v z}{l_w^{1/3} l_b^{2/3}}\right)\phi_w \phi_b^2. \tag{19}$$

The mixing-length models rest on the assumption that contributions from a single length-scale, which evolves with ζ, dominate the variance of the flow (l_w and l_b for the vertical velocity variance and buoyancy variance, respectively). This assumption implicitly requires that both kF_{ww} and kF_{bb} compensated spectra have distinct peaks associated with unique eddy sizes. In particular, it assumes that there are minimal contributions from low-wavenumber components. However, there is significant evidence to suggest that F_{bb} contains a region at low wavenumbers where $F_{bb} \sim k^{-1}$ under conditions ranging from mildly unstable to mildly stable (Kader and Yaglom, 1991; Katul *et al.*, 1995; Li *et al.*, 2015a,2016b). Therefore, kF_{bb} is constant in this region, meaning there is no distinct peak (Figure 1(d), solid line). Consistent with this statement, Kaimal and Finnigan (1994) note that the locations of peaks in kF_{bb} (from field experiments) are less predictable than those in kF_{ww} as stability conditions vary. Therefore, no single length-scale dominates the observed buoyancy variance. We now attempt to parsimoniously include these length-scales in the analysis.

2.4. *New model for ϕ_h*

In this section, we introduce an idealized form for F_{bb}, previously proposed in Li *et al.* (2015b), and use it to derive a new model for ϕ_h. Consider a new idealized spectrum for the buoyancy variance

$F_{bb}(k)$, which incorporates a low-wavenumber k^{-1} region:

$$F_{bb}(k) = \begin{cases} C_T N_b \epsilon^{-1/3} k^{-5/3} & \text{for } k \geq k_{ab}, \\ C_T N_b \epsilon^{-1/3} k_{ab}^{-2/3} k^{-1} & \text{for } k_{ab} > k \geq k_\Lambda, \\ C_T N_b \epsilon^{-1/3} k_{ab}^{-2/3} k_\Lambda^{-1} & \text{for } k < k_\Lambda, \end{cases} \quad (20)$$

where k_{ab} and k_Λ are transition wavenumbers (Figure 1(b), solid line). The k^{-1} region likely appears in the high Reynolds number limit. When applied to a low Reynolds number DNS, as in this study, it should be considered an 'effective' k^{-1} region, which better captures effects of large eddies to first-order. Integrating Eq. (20) between $k = 0$ and $k = \infty$, defining $k_{ab} = 2\pi/l_b$ and $k_\Lambda = 2\pi/\Lambda$, substituting Eq. (15) and rearranging gives

$$N_b = \frac{2^{3/2}\pi}{(5C_K)^{1/2}} \frac{\sigma_w \sigma_b^2}{C_T l_w^{1/3} l_b^{2/3} \left\{ \frac{5}{2} + \log\left(\frac{\Lambda}{l_b}\right) \right\}}. \quad (21)$$

Substituting this into Eq. (13) and rearranging gives

$$\phi_h\left(\frac{z}{L}\right) = \left(\frac{2^{5/2}\pi}{5^{3/2} C_T C_K^{1/2}}\right)\left(\frac{1}{1+\frac{2}{5}\log\left(\frac{\Lambda}{l_b}\right)}\right) \times \left(\frac{k_v z}{l_w^{1/3} l_b^{2/3}}\right) \phi_w \phi_b^2. \quad (22)$$

Comparing Eqs (19) and (22), the impact of the k^{-1} region on ϕ_h is the introduction of an extra positive factor

$$\left\{1 + \frac{2}{5}\log\left(\frac{\Lambda}{l_b}\right)\right\}^{-1},$$

which introduces sensitivity to the larger length-scale Λ. This factor reduces ϕ_h, relative to the mixing-length model, and does so to a greater extent as the ratio Λ/l_b increases.

3. Sensitivity test based on field measurements

To complement the DNS analysis, in this section we use available field experiment data to test our spectral models of ϕ_m and ϕ_h. We perform sensitivity analyses for relevant variables where field experiment measurements are unavailable or subject to significant uncertainty. The aim is to determine whether or not our models for ϕ_m and ϕ_h are consistent with available field measurements.

The field measurements are obtained from a range of previous studies, which are briefly summarized here. We use measurements of $\phi_w(z/L)$ and $\phi_b(z/L)$ estimated by Bradley and Antonia (1979) using data from the 1976 International Turbulence Comparison Experiment (ITCE). We also use values of ϕ_w and ϕ_b estimated by Kader and Yaglom (1990) using data obtained from the Tsimlyansk field station of the Moscow Institute of Atmospheric Physics, over the summers of 1981 to 1987. Additional estimates of ϕ_b were obtained from Bradley and Antonia (1979) based on observations from the 1972 Minnesota field experiment, described in Lynch and Bradley (1974); and from Bradley and Antonia (1979) based on observations from the 1968 Kansas field experiment, described in Haugen *et al.* (1971). We use measurements of $\phi_m(z/L)$ and $\phi_h(z/L)$ estimated in Businger *et al.* (1971) using observations from the Kansas field experiment; and estimates published in Högström (1988) based on observations from a field site in Uppsala, Sweden; and estimates published in Brutsaert (1982) based on observations from several field sites in New South Wales, Australia, described in Dyer and Hicks (1970). Finally, measurements of peaks of the compensated spectra of vertical velocity variance and buoyancy variance are obtained from values published in Businger *et al.* (1971) based on observations from the Kansas field experiment.

The required model inputs are ϕ_w, ϕ_b, l_w, l_b and Λ. Empirical relations for ϕ_w and ϕ_b as functions of ζ are available from previous field studies. Since there is considerable scatter around these relations, we assess the sensitivity of our models to these relations, using field experiment measurements to set the bounds of the sensitivity analysis. The bounds are shown in Figure 2. While the empirical relation for ϕ_w appears to be unbiased, the empirical relation for ϕ_b is negatively biased compared to measurements from multiple field experiments. This illustrates the importance of considering the effects of variability around the empirical relations for ϕ_w and ϕ_b with a sensitivity analysis.

The length-scales l_w, l_b and Λ are estimated from observed peaks in the compensated spectra of vertical velocity variance and buoyancy variance. Specifically, we assume that l_w and l_b both scale with distance from the wall such that $l_w = \alpha_w z$ and $l_b = \alpha_b z$, for some α_w and α_b which can both vary with ζ. This assumption is justified based on observations and theory discussed in the previous section, and is necessary to remove z-dependence in our models of ϕ_m and ϕ_h. Typically, the observed peak in the compensated spectrum is reported as a non-dimensionalized frequency f corresponding to the peak of the normalized spectrum. Specifically, $f = nz/U$ (where n is the frequency), which can be linked to a wavenumber using Taylor's frozen turbulence hypothesis (Taylor, 1938) via the relation $f = kz/2\pi$. In our model, the vertical velocity variance spectrum peaks at a wavenumber $k = 2\pi/l_w$. Therefore, the peak in the spectrum of vertical velocity variance occurs at a non-dimensionalized frequency $f_{mw} = z/l_w = \alpha_w^{-1}$. Observations of f_{mw} are shown in Figure 2, along with bounds for the sensitivity analysis. We further assume that $l_w = l_b$ and, therefore, $\alpha_w = \alpha_b$. Finally, in the presence of a k^{-1} scaling regime, the compensated buoyancy variance spectrum does not have a unique peak (Figure 1(d), solid line). A previous field study (Kaimal *et al.*, 1972) reported estimates of peaks in the compensated buoyancy variance spectra ($f_{m\theta}$, Figure 2), but it has since been noted that these apparent peaks are difficult to identify (Kaimal and Finnigan, 1994). It is plausible that the apparent 'peaks' in the spectrum corresponded to the length-scale Λ, i.e. $f_{m\theta} \approx z/\Lambda$. However, given the uncertainty in the relation between $f_{m\theta}$ and Λ, we impose very wide uncertainty bounds on $f_{m\theta}$ in our sensitivity analysis.

By varying ϕ_w, ϕ_b, f_{mw} and $f_{m\theta}$ within the ranges shown in Figure 2, we model plausible ranges for ϕ_m and ϕ_h. The results of this sensitivity analysis are shown in Figure 3. Both modelled ϕ_m and ϕ_h are quite sensitive to reasonable deviations from the assumed relations above. The proposed mixing-length model for ϕ_m (Eq. (16)) is not obviously inconsistent with measurements, since the measurements overlap the plausible model predictions of ϕ_m. In contrast, the mixing-length model of ϕ_h (Eq. (19)) is clearly inconsistent with most of the measurements, since most of the measurements do not overlap the plausible model predictions for ϕ_h, even after accounting for significant uncertainty in model inputs (l_w, l_b, ϕ_w, ϕ_b). The mixing-length model for ϕ_h consistently overestimates observed ϕ_h. However, including contributions from the larger length-scale Λ appears to resolve the inconsistency, since the plausible range of model predictions from Eq. (22) overlap with observed ϕ_h.

These results, which are based solely on field experiment measurements, demonstrate that large eddies (corresponding to the length-scale Λ, and included in Eq. (22) but not Eq. (19)) appear to play a necessary role in determining the shape of ϕ_h, a result that is inconsistent with MOST. The presented analysis establishes that the mixing-length model of ϕ_h is deficient, but is unable to conclusively validate the performance of our alternative model (Eq. (22)) due to uncertainties in the field measurements. In the next section, we use a high-resolution simulation of an idealized ASL to more precisely test these mechanisms.

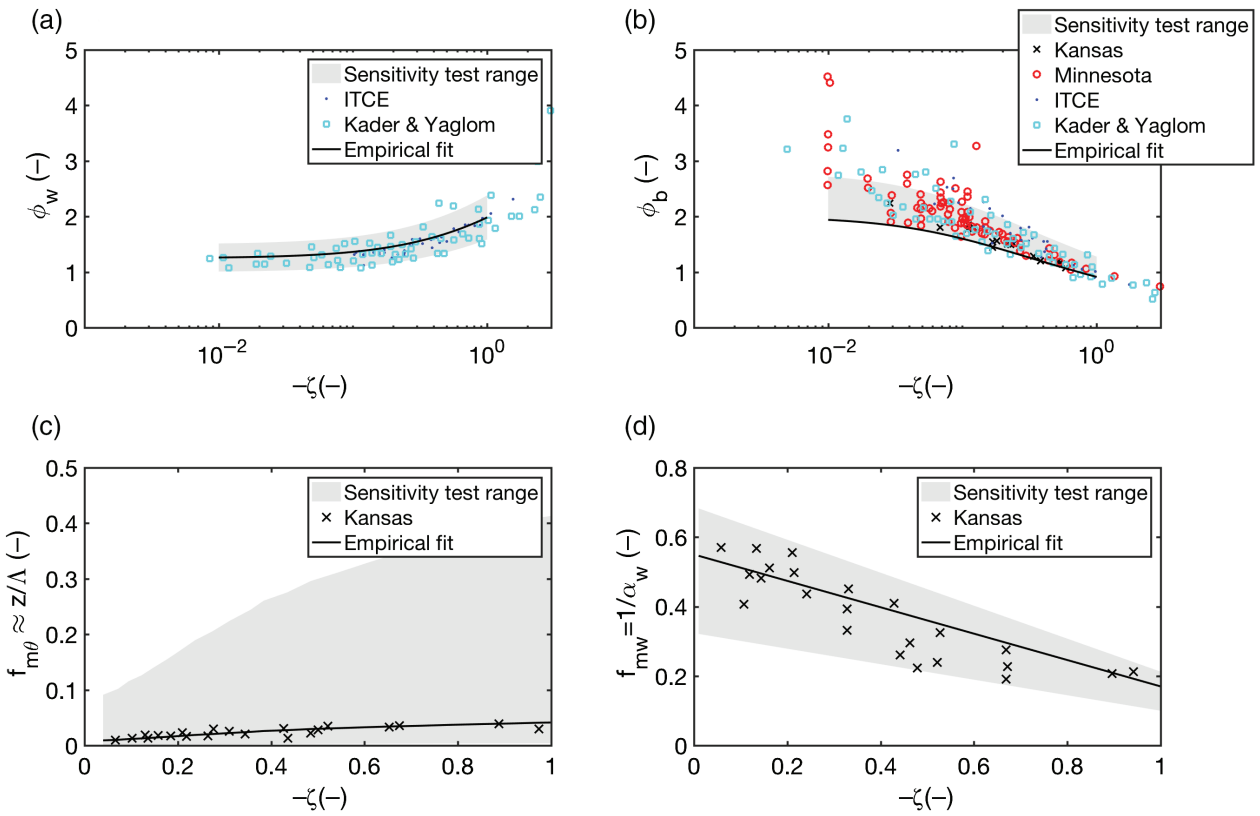

Figure 2. Plausible ranges of variables (a) ϕ_w, (b) ϕ_b, (c) z/Λ, and (d) $1/\alpha_w$) used in the sensitivity analysis, based on field measurements. ITCE and Minnesota measurements obtained from Bradley and Antonia (1979). Kansas observations obtained from Bradley and Antonia (1979), Businger *et al.* (1971), and Kaimal *et al.* (1972). Observations from a range of studies were also obtained from Kader and Yaglom (1990). The empirical fits are standard functional forms fitted to the data in previous studies (Kaimal and Finnigan, 1994). [Colour figure can be viewed at wileyonlinelibrary.com].

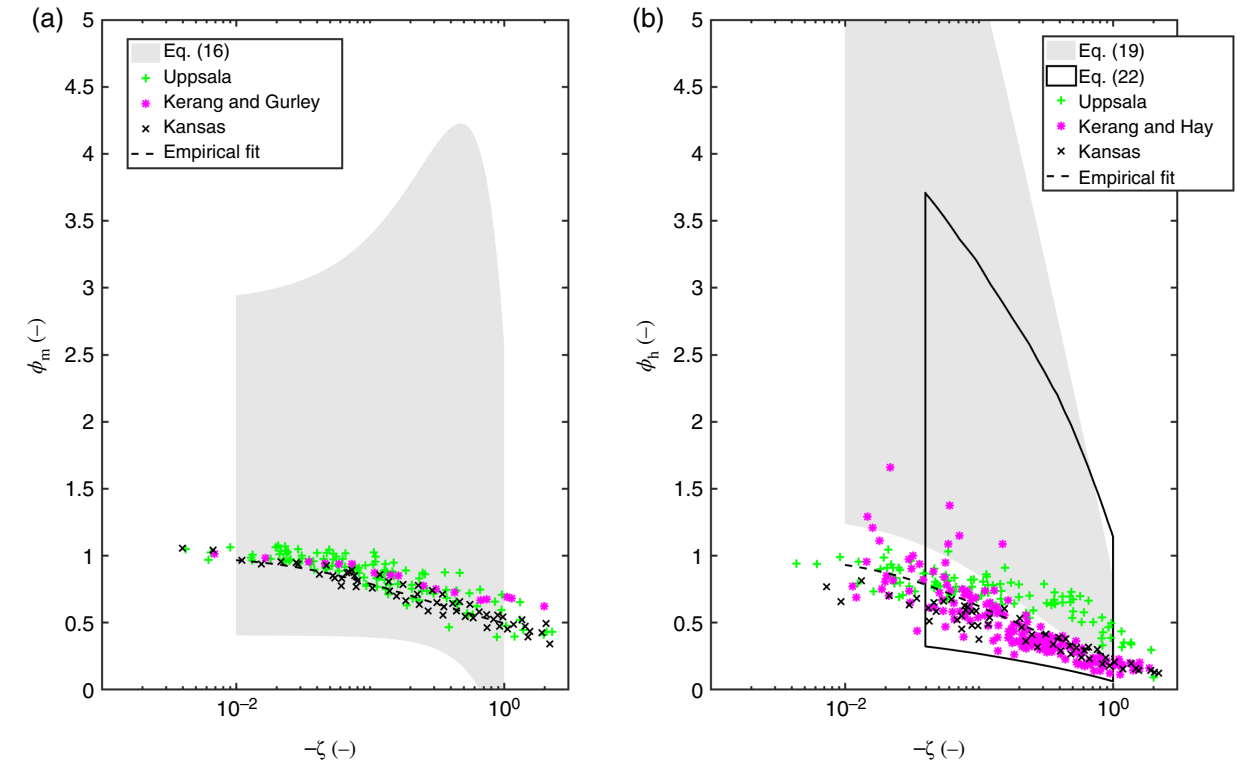

Figure 3. Sensitivity tests of proposed models for (a) ϕ_m (Eq. (16)) and (b) ϕ_h (Eqs (19) and (22)), with sensitivity ranges of variables shown in Figure 2. (a) Reasonable variations in parameters for the mixing-length model of ϕ_m (Eq. (16)) reproduce field measurements. (b) In contrast, the mixing-length model for ϕ_h (Eq. (19)) cannot reproduce the majority of field measurements. The model for ϕ_h that includes contributions from a larger length-scale Λ (Eq. (22)) is able to reproduce field measurements. Kansas observations obtained from Bradley and Antonia (1979), Businger *et al.* (1971), and Kaimal *et al.* (1972). Observations from a range of studies were also obtained from Kader and Yaglom (1990). Uppsala observations obtained from Högström (1988). Kerang, Gurley and Hay observations obtained from Brutsaert (1982). The empirical fits are standard functional forms fitted to the data in previous studies (Kaimal and Finnigan, 1994). [Colour figure can be viewed at wileyonlinelibrary.com].

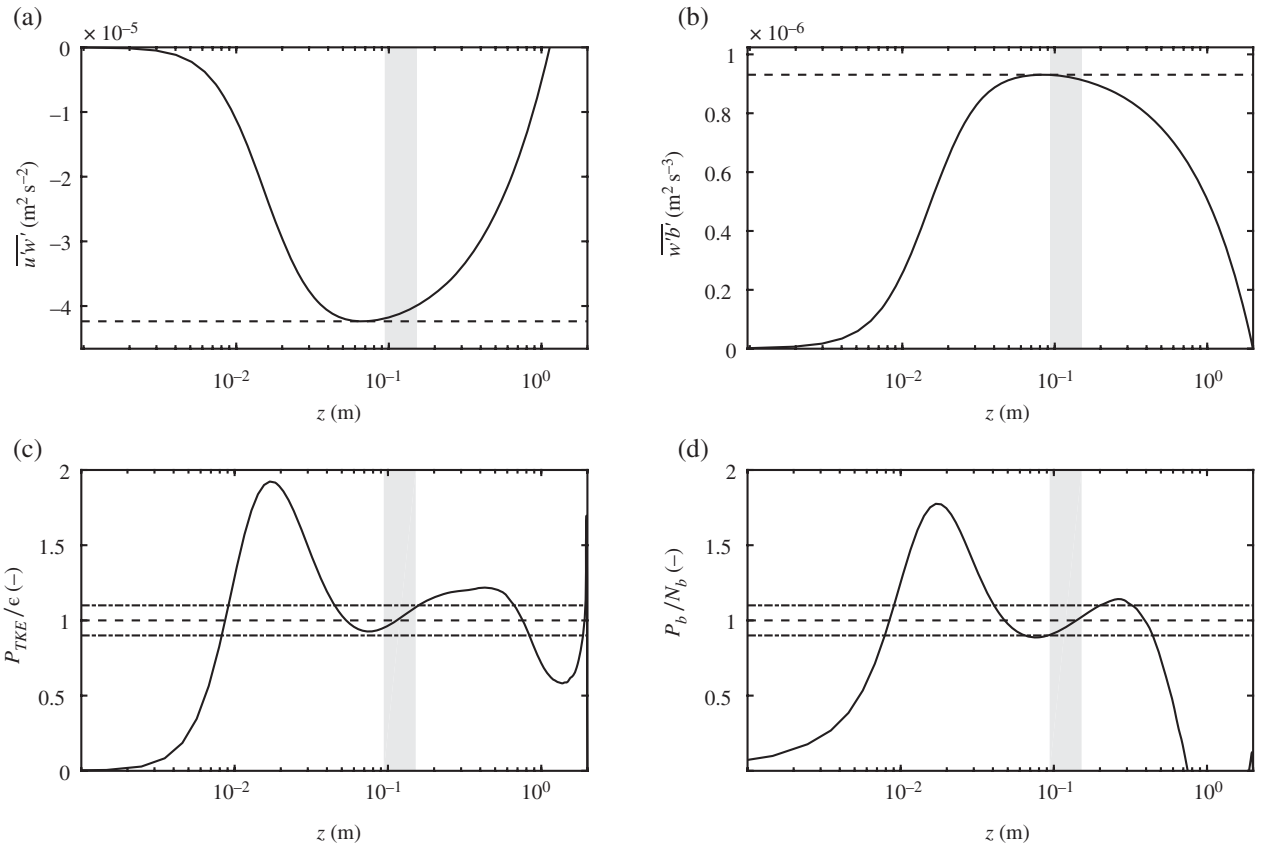

Figure 4. Profiles of DNS (a) $\overline{u'w'}$ (solid line) and estimated u_* (dashed line), (b) $\overline{w'b'}$ (solid line) and estimated b_* (dashed line), (c) ratio of TKE production $P_{\mathrm{TKE}} = -\overline{u'w'}\mathrm{d}U/\mathrm{d}z + \overline{w'b'}$ to dissipation rate ϵ (solid line), with reference lines showing perfect equilibrium ($P_{\mathrm{TKE}} = \epsilon$, dashed line) and ±10% bounds (dot-dashed lines), (d) ratio of half the buoyancy variance production $P_b = \overline{w'b'}\mathrm{d}B/\mathrm{d}z$ to half the dissipation rate N_b (solid line), with reference lines showing perfect equilibrium ($P_b = N_b$, dashed line) and ±10% bounds (dot-dashed lines). Shaded regions in all plots denote the estimated 'constant-flux' region relevant to MOST.

4. Simulation

To test the models for ϕ_m and ϕ_h derived earlier for mildly unstable conditions (i.e. conditions where the k^{-1} power law may appear in buoyancy spectra), a high-resolution simulation of an idealized ASL is conducted. A DNS of a steady heated channel flow is performed using the computational fluid dynamics code MicroHH (http://microhh.org, accessed 1 June 2017; van Heerwaarden *et al.*, 2017). Effects of non-stationarity, surface roughness and entrainment are ignored in these simulations. This is a common idealized configuration used in studying the atmospheric boundary layer (ABL; e.g. Stevens, 2000), and can be interpreted as a quasi-steady boundary layer over a smooth air – water interface, with strong stability in the free troposphere. Furthermore, this configuration can be used to test the hypotheses that non-stationarity, surface roughness and/or entrainment play an essential role in the dissimilarity of ϕ_m and ϕ_h in unstable surface layers. If the Reynolds analogy breakdown is observed in the DNS, then the dissimilarity cannot be solely due to non-stationarity, surface roughness and/or entrainment. Other factors must also play a significant role.

The dimensions of the domain are 9.4 m×9.4 m×2 m, discretized into 1152 × 1152 × 288 grid points. The equations are discretized in space using a fourth-order, energy-conserving scheme (Morinishi *et al.*, 1998). A third-order, adaptive step, Runge – Kutta scheme is used for time-stepping. Random perturbations are added to the u, v and w velocities to trigger turbulence. The flow is forced with a fixed mean streamwise velocity, resulting in a friction Reynolds number $Re_\tau = u_* R/\nu_0 = 687$, where $R = 1$ m is the channel half-width, and $\nu_0 = 10^{-5}\, m^2\, s^{-1}$ is the kinematic viscosity. The effects of the low Reynolds number on the analysis are investigated further in the next section. The Prandtl number is $Pr_0 = \nu_0/\kappa_0 = 1$, where κ_0 is the thermal diffusivity. Periodic boundary conditions are applied in both horizontal dimensions. No-slip boundary conditions are imposed at both the upper and lower boundaries. A constant buoyancy flux boundary condition is imposed at the lower boundary (with constant flux $u_* b_* = 10^{-6}\,\mathrm{m^2\,s^{-3}}$), with a zero-flux boundary condition at the upper boundary; hence, buoyancy accumulates in the channel over time. However, the flow reaches a quasi-steady state, i.e. the variable $\Theta(z) = B(0,t) - B(z,t)$ becomes constant in time.

Flow statistics, including the spectra, were estimated at a fixed height and time using the modelled w and b fields. The statistics were then averaged across a sufficiently long time period to include contributions from large-scale flow structures induced by heating.

MOST applies to the 'constant flux layer', where $\overline{u'w'}$ and $\overline{w'b'}$ do not vary appreciably with height. Furthermore, the TKE and buoyancy variance budgets are assumed to be equilibrated in this region, with production balancing dissipation. Figures 4(a) and (b) show profiles of $\overline{u'w'}$ and $\overline{w'b'}$, respectively. Both profiles exhibit a fairly broad peak around $z = 0.07$ m. In atmospheric studies, the friction velocity is often estimated from eddy covariance measurements of $\overline{u'w'}$ in the constant flux layer (Högström, 1988; Kaimal and Finnigan, 1994). We therefore estimate the friction velocity as

$$u_* = \sqrt{-\overline{u'w'}|_{z=0.07\,\mathrm{m}}}.$$

This value is only an approximation of the surface friction velocity

$$u_\tau = \sqrt{-\overline{u'w'}|_{z=0\,\mathrm{m}}}.$$

In our DNS, $u_\tau > u_*$ (not shown), consistent with field measurements using stress plates (Haugen *et al.*, 1971). To ensure consistency with field measurements, we use u_* rather than u_τ in this study.

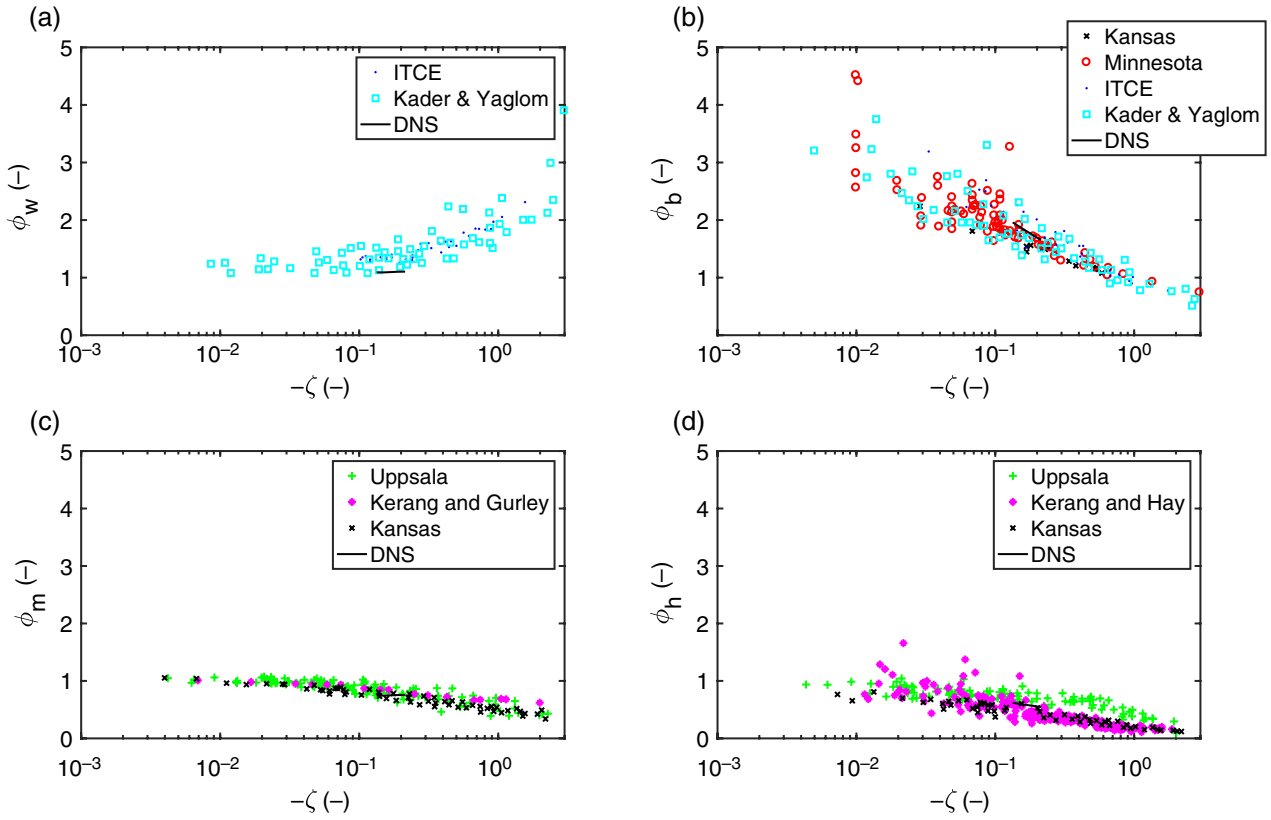

Figure 5. Monin – Obukhov Similarity Theory (MOST) functions under unstable conditions, estimated from field experiments and the DNS used in this study: (a) ϕ_w, (b) ϕ_b, (c) ϕ_m and (d) ϕ_h. ITCE and Minnesota measurements are obtained from Bradley and Antonia (1979). Kansas observations are obtained from Bradley and Antonia (1979) and Businger *et al.* (1971). Uppsala observations are obtained from Högström (1988). Kerang, Gurley and Hay observations are obtained from Brutsaert (1982). Observations from a range of studies were also obtained from Kader and Yaglom (1990). [Colour figure can be viewed at wileyonlinelibrary.com].

Figures 4(c) and (d) show the constant-flux layer in the DNS approximately coincides with a region where the TKE and $\overline{b'^2}$ budgets are reasonably well equilibrated (i.e. production balances dissipation). We constrain our analyses to the single contiguous region where production balances dissipation in both TKE and $\overline{b'^2}$ budgets to within ±10% ($0.13 \leq -z/L \leq 0.21$). While this 10% variation introduces some error into the analysis, we show later that the effects are fairly minor. Moreover, from previous DNS studies of neutral channel flow, it appears that production and dissipation may never exactly balance in this layer, even at much higher Reynolds number (Lee and Moser, 2015). While the constant-flux layer in the DNS is relatively small, it spans a range of mildly unstable conditions that have received relatively little attention.

We estimate the length-scales l_w, l_b and Λ from the DNS spectra. We also fit the parameters C_T and C_K rather than using the values obtained from previous experiments. This is because the DNS is at a low Reynolds number, and using values from high Reynolds number experiments results in a substantial overestimation of the spectra. To fit the idealized F_{ww} spectrum, we first choose the value of C_K to be the value such that the curve $F_{ww}(k) = C_K \epsilon^{2/3} k^{-5/3}$ lies tangent to the DNS spectrum. Second, integrating this idealized spectrum gives

$$k_{aw} = \frac{2\pi}{l_w} = 2\pi \left(\frac{2}{5C_K} \right)^{-3/2} \frac{\epsilon}{\sigma_w^3}, \tag{23}$$

allowing l_w to be estimated from the estimated value of C_K, and the DNS ϵ and σ_w fields. Using a similar approach for F_{bb}, we obtain

$$k_{ab} = \frac{2\pi}{l_b} = 2\pi \left(\frac{2}{5C_T} \right)^{-3/2} \frac{N_b^{3/2}}{\sigma_b^3 \epsilon^{1/2}}. \tag{24}$$

In addition, we fit the new idealized spectrum for F_{bb}, which contains a k^{-1} region. We first choose the value of C_T to be the value such that the curve $F_{bb}(k) = C_T N_b \epsilon^{-1/3} k^{-5/3}$ lies tangent to the DNS spectrum. Second, we choose the value of $k_{ab} = 2\pi/l_b$ to be the value such that $C_T N_b \epsilon^{-1/3} k_{ab}^{-2/3}$ lies tangent to the DNS compensated spectrum $kF_{bb}(k)$. Finally, integrating the idealized spectrum and rearranging gives

$$\Lambda = \frac{l_b}{2} \exp\left(\frac{(2\pi)^{2/3} \sigma_b^2}{C_T l_b^{2/3} N_b \epsilon^{-1/3}} - \frac{5}{2} \right), \tag{25}$$

allowing Λ to be determined from the estimated values of C_T and l_b, and the DNS σ_b, N_b and ϵ fields.

There are important differences between a low Reynolds number heated channel flow, and an ASL. We assess the impact of this difference on our analysis by comparing MOST statistics, spectra, and integral length-scales estimated from field experiments with those estimated from the DNS. The integral length-scale of the vertical velocity variance is defined as

$$I_w = \int_0^\infty \rho_w(s)\, \mathrm{d}s = \frac{\pi}{2} \frac{F_{ww}(0)}{\sigma_w^2}, \tag{26}$$

where $\rho_w(s)$ is the vertical velocity autocorrelation function. DNS I_w is estimated using the $F_{ww}(0)$ and σ_w DNS fields. Integral length-scales of the buoyancy variance (I_b) and streamwise velocity variance (I_u) are defined and estimated in a similar fashion.

5. Results

Estimates of several MOST functions from field experiments are compared with those estimated from the DNS (Figure 5). All of the DNS-estimated MOST functions lie within the scatter of estimates from field experiments. For ϕ_w, the DNS estimate is at the low end of the range observed in field experiments.

DNS-estimated spectra are also compared to those estimated from field experiments (Figure 6). Both the DNS F_{ww} and F_{bb}

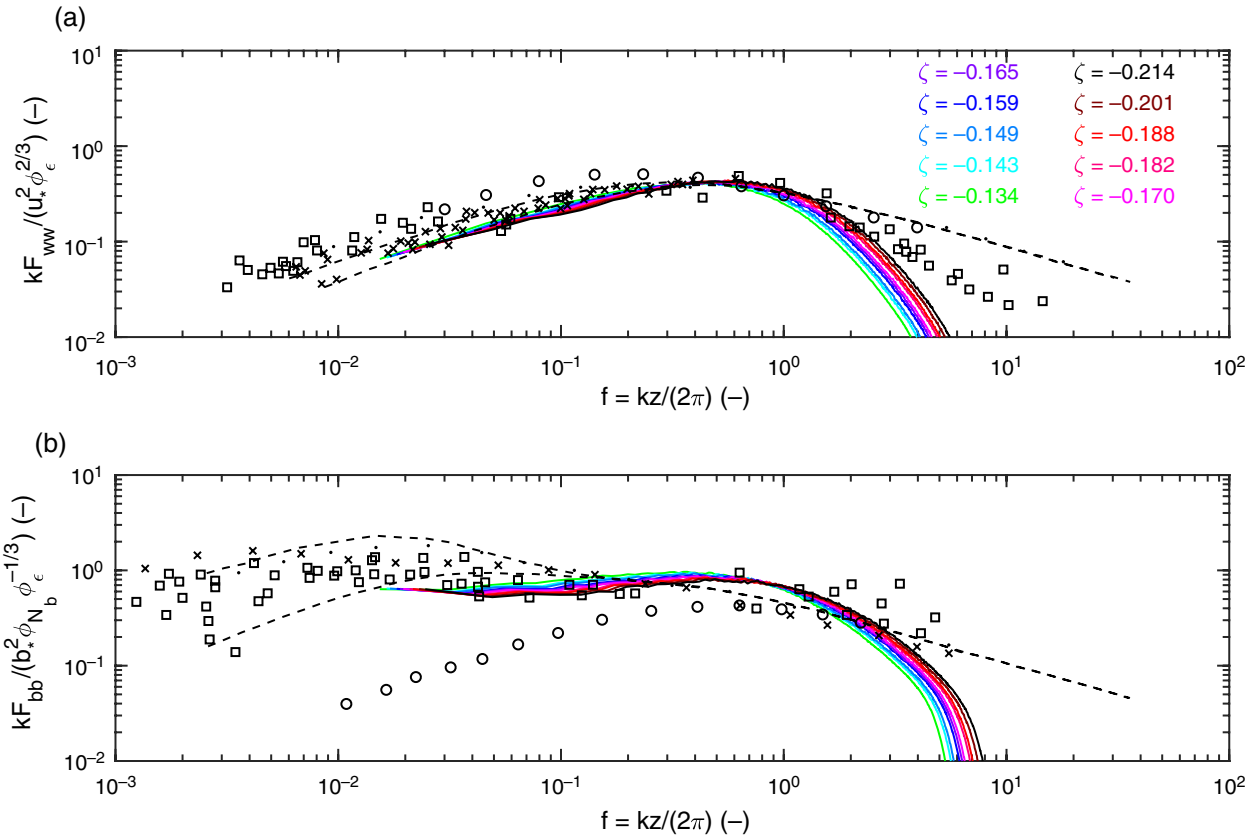

Figure 6. Comparison of normalized DNS spectra (coloured lines) with field experiment measurements. The non-dimensionalized TKE dissipation rate is defined $\phi_\epsilon = kz\epsilon/u_*^3$. (a) Smoothed and averaged spectra at Cedar Hill (circles; Busch and Panofsky, 1968), smoothed and averaged spectra at Kansas (black dashed lines, $0.1 \leq -\zeta \leq 0.3$, Kaimal *et al.*, 1972); individual measurements at Kansas (black crosses; $0.1 \leq -\zeta \leq 0.3$; Kaimal *et al.*, 1972), individual measurements over a tidal flat (black squares; Miyake *et al.*, 1970), and individual measurements at Vancouver (black dots; Busch and Panofsky, 1968). (b) Smoothed and averaged spectra at Kansas (black dashed lines, $0 \leq -\zeta \leq 2$; Kaimal *et al.*, 1972), measurements from BOMEX (black circles; $0.11 \leq -\zeta \leq 0.27$; Phelps and Pond, 1971), Ladner (black crosses; McBean, 1970), San Diego (black dots; $0.12 \leq -\zeta \leq 0.20$; Phelps and Pond, 1971), and over a tidal flat (black squares; Miyake *et al.*, 1970). All field experiment data obtained from Kaimal *et al.* (1972). [Colour figure can be viewed at wileyonlinelibrary.com].

spectra exhibit small inertial ranges, decaying more rapidly than field-observed spectra. This is a result of the low Reynolds number of the DNS. However, other key features are well-replicated. For F_{ww}, the DNS spectral peak matches that of field measurements. While there is considerable scatter at low frequencies, the DNS spectra match the Kansas data at low frequencies well. For F_{bb}, there is considerable scatter in field measurements, particularly at low frequencies. In particular, the Barbados Oceanographic and Meteorological Experiment (BOMEX) measurements differ substantially. Phelps and Pond (1971) suggest this may be due to radiation effects, although the reasons for the discrepancy are still unclear (Kaimal *et al.*, 1972). The DNS F_{bb} spectra lie within the observational scatter, for low wavenumbers excluding the inertial and viscous ranges. Both the normalized DNS F_{bb} spectra, and those from field measurements, exhibit a relatively flat region for $f < 10^0$, which is not present in the F_{ww} spectra. Overall, the DNS-estimated spectra are consistent with measurements, both in terms of magnitude and shape. An exception to this is in the inertial range, which is small in the DNS due to the low Reynolds number, resulting in a more rapid drop at higher frequencies in the DNS spectra.

DNS-estimated integral length-scales are compared to those estimated from a field experiment over a lake (Figure 7). The DNS-estimated ratio I_b/I_w matches field measurements well. While the range of stabilities ζ considered in the DNS simulations is relatively small, it covers a range where I_w is growing most rapidly relative to I_b. The DNS-estimated ratio I_u/I_w does not fit measurements as well as I_b/I_w, although the DNS estimates lie within the 95% confidence interval of the field measurements (not shown). This discrepancy is possibly due to the influence of the side walls in the DNS, limiting the development of large structures in the horizontal plane. Nevertheless, the streamwise and spanwise domain lengths for the DNS used in this study are larger than those used in comparable studies (Iida and Kasagi, 1997; Dong and Lu, 2005; Zonta and Soldati, 2013; Garai *et al.*, 2014). The DNS is able to reproduce the relative evolution of integral length-scales of buoyancy and vertical velocity variance, which are most relevant to this study.

Idealized spectra for F_{ww} and F_{bb} are fit to the DNS-observed spectra, and compared for a few example values of $-\zeta$ in Figure 8. Overall, the idealized forms capture the first-order features of the spectra. For F_{ww}, the spectra are underestimated at low frequencies, and overestimated at high frequencies. Nevertheless, the spectral peaks, which define l_w, are well-approximated by the idealized form. In contrast, for F_{bb}, the DNS-observed spectra are not well-approximated unless a k^{-1} region is included in the idealized form. Even then, high wavenumbers are overestimated, and low wavenumbers are underestimated. Furthermore, the k^{-1} region in the idealized form misses some curvature in the observed spectra. Still, the k^{-1} idealized form captures, to leading order, the fact that F_{bb} has significant contributions from low wavenumbers, and the location where the k^{-1} region begins.

The estimated length-scales l_w, l_b and Λ are compared with field measurements of $f_{\max}$, the non-dimensionalized frequency corresponding to the maximum of the normalized spectrum (Figure 9). Recall that the non-dimensionalized frequency $f = nz/U$ (where n is the frequency) is linked to the wavenumber by Taylor's frozen turbulence hypothesis (Taylor, 1938), via the relation $f = kz/2\pi$. Therefore, for our model of F_{ww}, $f_{\max} = z/l_w$. Models and field experiments yield consistent estimates, in the range of 0.5 – 0.8. Both estimates of l_w and l_b are reasonably consistent with field measurements. The estimated l_b is larger than the estimated l_w. The field measurements also show that $f^{\theta}_{\max}$ is substantially lower than $f^{w}_{\max}$. This demonstrates the significance of low-wavenumber contributions to the buoyancy variance. For the idealized model of F_{bb}, there is no unique maximum, with the

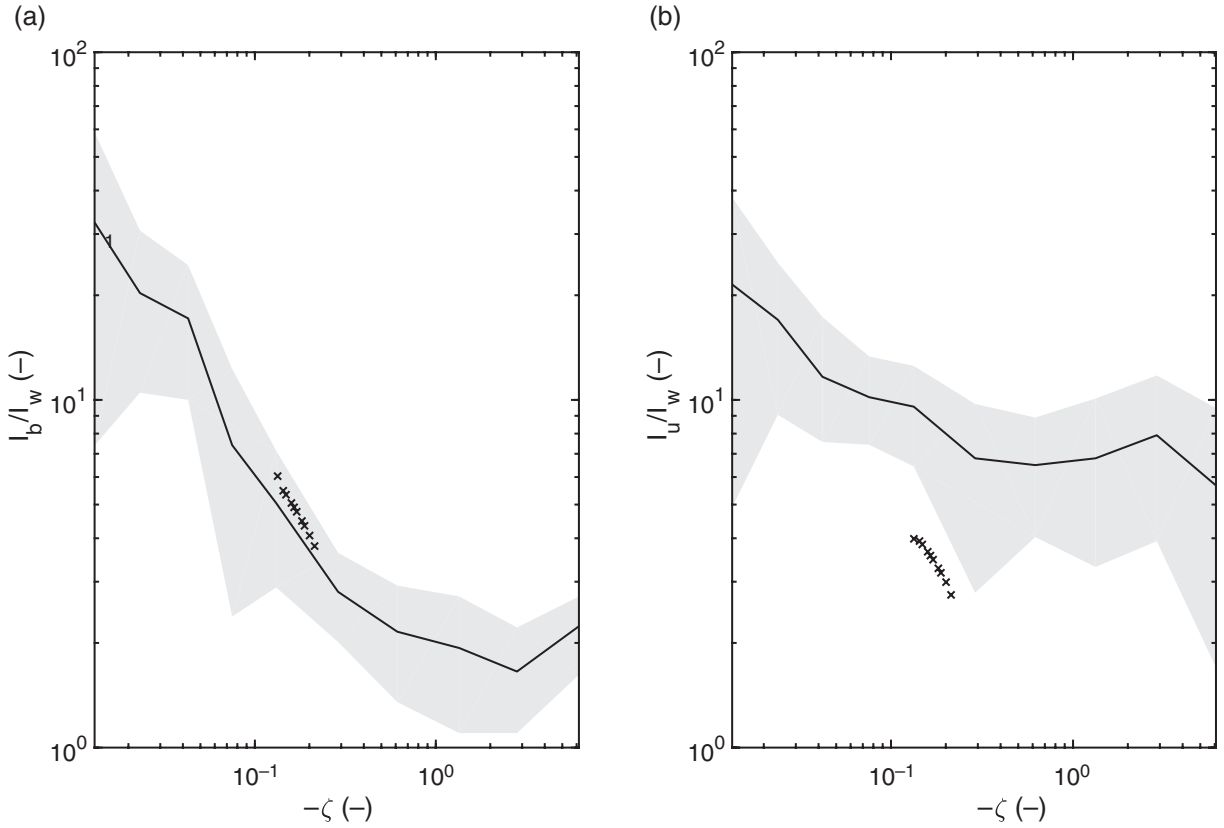

Figure 7. (a) Ratio of integral length-scales of buoyancy variance (I_b) to vertical velocity variance (I_w), estimated from the DNS (crosses), and from ASL measurements over a lake (Vercauteren *et al.*, 2008; Li *et al.*, 2012). The shaded region is ± one standard deviation from the estimated mean (black solid line). (b) is as (a) but for ratio of streamwise velocity variance (I_u) to vertical velocity variance (I_w).

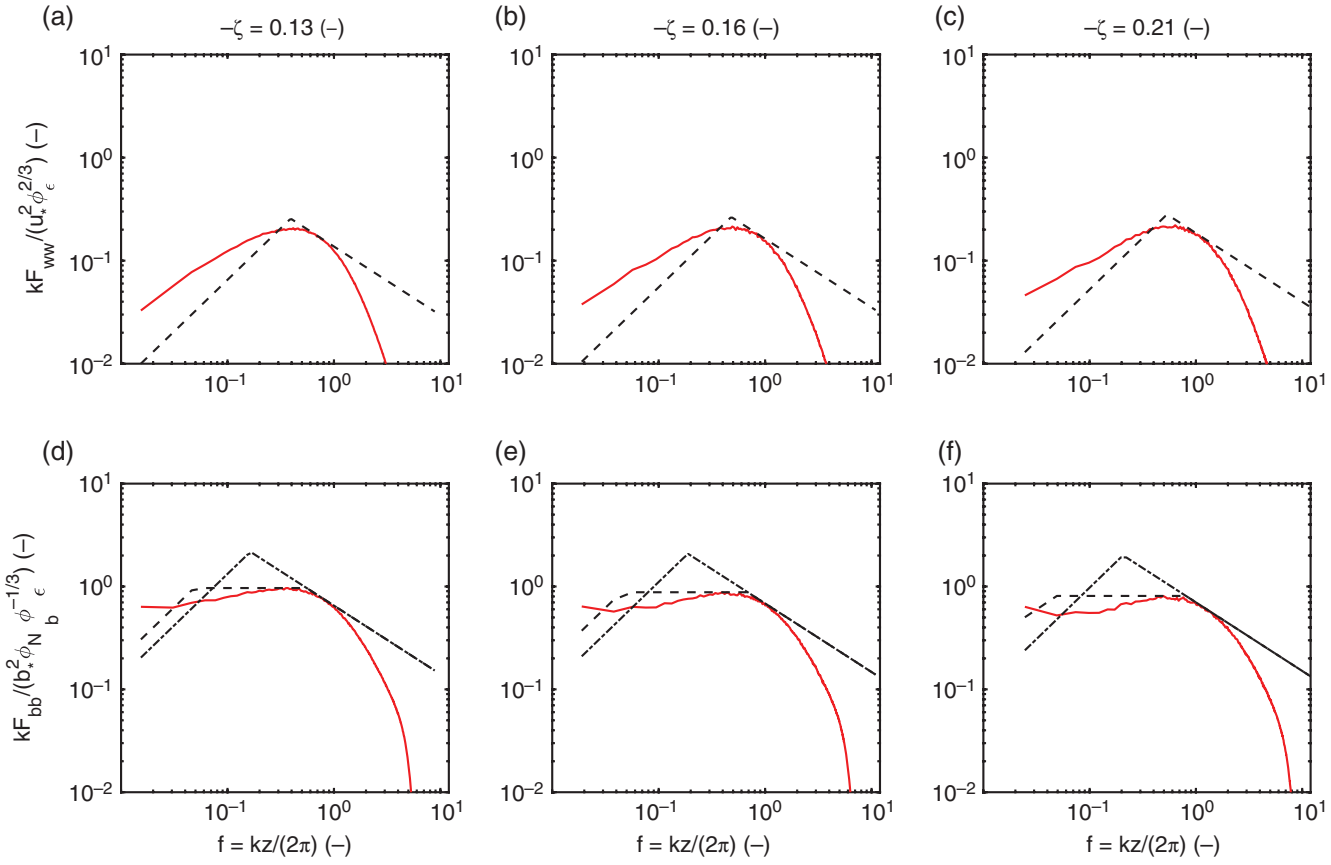

Figure 8. Idealized spectra (black lines) fitted to observed spectra (red solid lines): for (a) – (c) vertical velocity variance (the idealized form given by Eq. (14)), and for (d) – (e) buoyancy variance (the idealized form given by Eqs (17) (dot-dashed line) and (20) (dashed line)). [Colour figure can be viewed at wileyonlinelibrary.com].

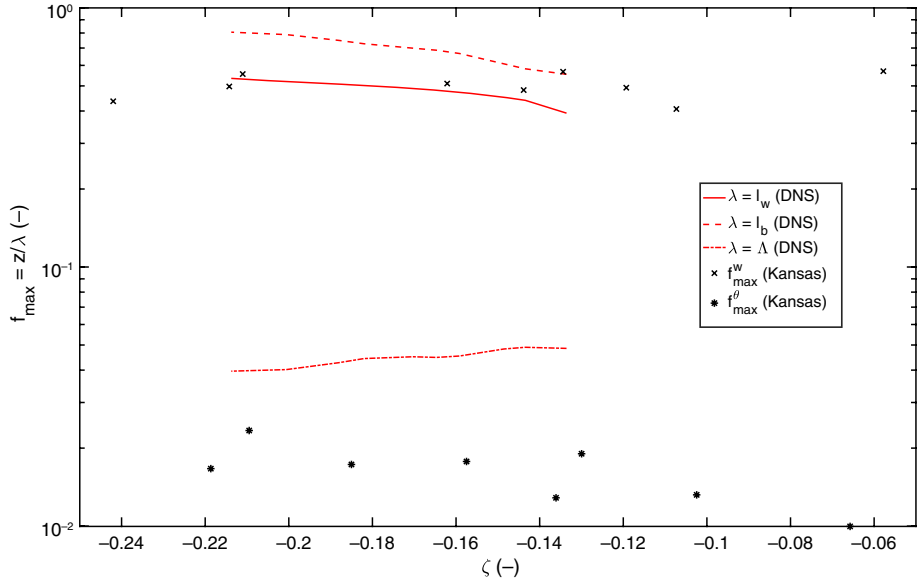

Figure 9. Location of spectral peaks (f_{max}) reported from field experiments, and idealized spectra calibrated to DNS, and their dependence on stability. Field observations from the Kansas field experiment are obtained from Kaimal *et al.* (1972). f^w_{max} and f^θ_{max} are the observed spectral peaks of the vertical velocity variance and potential temperature spectra, respectively. [Colour figure can be viewed at wileyonlinelibrary.com].

spectrum reaching its maximum in the interval $z/\Lambda \leq f \leq z/l_b$. However, if z/Λ is considered as an imperfect proxy for f^θ_{max}, a much closer agreement emerges, compared to using $f^\theta_{max} = z/l_b$.

DNS-estimated stability correction functions (ϕ_m and ϕ_h) are now compared with modelled values in Figure 10. The modelled function ϕ_m estimated using Eq. (16) matches the DNS-estimated function reasonably. Both DNS and model estimates agree closely with the Businger – Dyer function (Businger *et al.*, 1971). Correcting for deviations from model assumptions (using Eq. (A5)) results in only minor differences (see Appendix). For ϕ_h, two models are presented. The first (Eq. (19)) does not include low-wavenumber contributions. This model severely overestimates ϕ_h. The second model includes low-wavenumber contributions (Eq. (20)), and fits the DNS ϕ_h reasonably. Deviations from other model assumptions are shown to have a minor effect on modelled ϕ_h, compared with the effects of neglecting low-wavenumber contributions. This implies that large eddies (corresponding to large length-scales approximated in this analysis by Λ) play a fundamental role in determining the shape of ϕ_h, consistent with the sensitivity analysis using field measurements in section 3. While this has long been recognized under strongly unstable conditions – sometimes referred to as 'local free convection' (Wyngaard *et al.*, 1971; Businger, 1973; Zilitinkevich *et al.*, 2006) – it has not been recognized as significant under mildly unstable conditions such as those considered here.

6. Discussion

In this section, the results in the previous section are compared with previous studies in the literature. Particular attention is devoted to the k^{-1} region in the buoyancy variance spectrum, focusing on its stability-dependence, its implications for the development of mixing-length models, and to its role in observed departures from MOST.

6.1. *Comparison with previous studies*

While several DNSs of the stably stratified (e.g. van de Wiel *et al.*, 2008; Chung and Matheou, 2012; Ansorge and Mellado, 2014; He and Basu, 2015) and free convective (e.g. van Heerwaarden *et al.*, 2014; Garcia and Mellado, 2014; Mellado *et al.*, 2015; van Heerwaarden and Mellado, 2016) boundary layer exist in the literature, relatively few DNS studies of an idealized, mildly unstable ASL exist. It is this gap that the DNS results here attempt to fill. Furthermore, while the Reynolds number is low compared to the ASL, it is higher than comparable DNSs in the literature (Iida and Kasagi, 1997; Dong and Lu, 2005; Zonta and Soldati, 2013; Garai *et al.*, 2014). Several heated, wall-bounded turbulent DNS studies have been performed at higher Reynolds numbers (Abe *et al.*, 2004; Zhu *et al.*, 2010; Zhang *et al.*, 2015), but these studies treat the temperature field as a passive scalar, neglecting the impacts of buoyancy on the flow velocities. Buoyancy-driven structures, such as thermals, are known to alter the turbulent velocity field (de Bruin *et al.*, 1993; Choi *et al.*, 2004; Li and Bou-Zeid, 2011), as evidenced by the key role of large eddies in our results, even under mildly unstable stratification.The DNS-estimated MOST functions compare reasonably with accepted MOST functions (Figure 5), albeit over a small range of ζ. The DNS-estimated spectra lack an extended inertial subrange, as expected, but are consistent with other features observed in field experiment data, such as the cut-off wavenumbers and low-wavenumber contributions (Figure 6). Finally, the relative evolution of the integral length-scales I_b and I_w with changing stability is correctly estimated by the DNS.

The DNS results are consistent with earlier studies implicating coherent structures in the dissimilarity of turbulent transport of heat and momentum (de Bruin *et al.*, 1993; Choi *et al.*, 2004; Li and Bou-Zeid, 2011). Several studies have suggested canopy impacts as a key factor in the dissimilar transport of heat and momentum (Katul *et al.*, 1997; Patton *et al.*, 2015). Canopy effects may well contribute, but we show in this study that they are not essential for the breakdown of the Reynolds analogy. Furthermore, while entrainment at the top of the boundary layer can cause deviations from MOST scaling (van de Boer *et al.*, 2014), it cannot be essential to the breakdown of the Reynolds analogy, since the DNS used here does not include any entrainment flux. Finally, the existence of dissimilarity is not solely an artifact of weak non-stationarity at large scales, or instrument filtering at fine scales infecting field experiments. The DNS is stationary and is subject to negligible measurement errors.

Several previous studies have proposed theories for the shapes of ϕ_m, and its dissimilarity with ϕ_h. One set of studies adopt a heuristic model of turbulent eddy fluxes, in which 'dominant', wall-attached eddies (Gioia *et al.*, 2010) transport turbulent excursions of velocity and temperature, with eddy overturning velocities determined by a simplified TKE budget (Katul *et al.*, 2011; Li *et al.*, 2012, 2016a; Salesky *et al.*, 2013). Li *et al.* (2012) propose an explanation for the dissimilarity in this framework, suggesting it is due to 'scale resonance' between fluctuations of vertical velocity and temperature. Another set of studies take

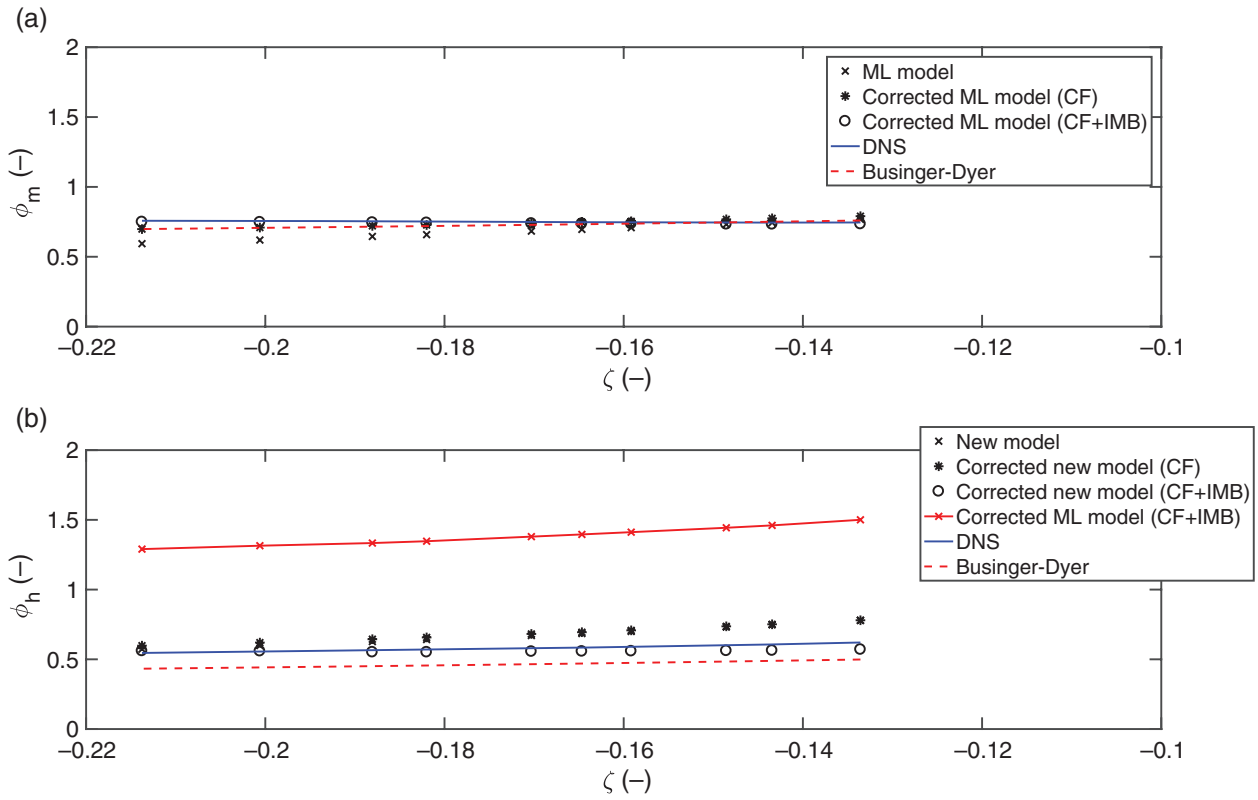

Figure 10. Modelled and DNS-estimated MOST stability-correction functions. (a) ϕ_m, estimated from the DNS and the mixing-length (ML) model given in Eq. (16), with and without corrections for the TKE budget imbalance (IMB) and violations of the constant flux assumption (CF), using Eq. (A5). (b) ϕ_h, estimated from the DNS, the ML model given in Eq. (19) and the new model given in Eq. (22), with and without corrections for the buoyancy variance budget imbalance (IMB) and violations of the constant flux assumption (CF), using Eqs (A6) and (A7). The Businger – Dyer curves, obtained empirically from fitting to field experiment data, are also given (Businger *et al.*, 1971). [Colour figure can be viewed at wileyonlinelibrary.com].

a different approach, based on cospectral budgets (Katul *et al.*, 2013, 2014; Li *et al.*, 2015a, 2015b). The cospectral budgets are solved by parametrizing pressure-strain and flux-transfer terms, allowing them to be solved for the turbulent Prandtl number $Pr_t = \phi_h/\phi_m$, in terms of ϕ_m, ζ and other parameters related to the spectra and cospectral budget parametrizations. In particular, Li *et al.* (2015b) use a cospectral budget framework to demonstrate the potential significance of the k^{-1} region in the temperature variance spectrum in explaining the dissimilarity between ϕ_h and ϕ_m, manifested as variations in $Pr_t = \phi_h/\phi_m$ with ζ. Using the same idealized spectra used in this study, they show that the dissimilarity increases as the k^{-1} region is given more prominence in the parametrized temperature variance spectrum. The DNS and idealized model also reproduce this result: as the k^{-1} region grows larger (i.e. Λ/l_b increases), ϕ_h decreases (Eq. (22)).

In contrast to previous studies, the approach proposed here solves for ϕ_m and ϕ_h explicitly, in terms of ϕ_w and ϕ_b and other parameters related to the spectra. This approach avoids the need for parametrizations of terms in the cospectral budget, which may be particularly ill-suited to low Reynolds numbers (McColl *et al.*, 2016). Our model can be viewed as describing the partitioning of kinetic (ϕ_w, F_{ww}) and potential energy (ϕ_b, F_{bb}) between the turbulent transport of momentum (ϕ_m) and heat (ϕ_h).

6.2. *Stability-dependence of k^{-1} region*

Over the small range of ζ considered in this study, Λ/l_b increases with increasing $-\zeta$ (Figure 9), suggesting the k^{-1} region grows with increasing instability. This appears to be in contrast to previous field experiments, where the k^{-1} region disappears as instability increases beyond some threshold (Kader and Yaglom, 1991; Katul *et al.*, 1995). There are several possible explanations for this inconsistency. First, the discrepancy may be real: indeed, the existence and stability-dependence of a k^{-1} region in the temperature variance spectrum is not yet well-established (Li *et al.*, 2015b). Second, the discrepancy may be real but small: the DNS spans a relatively small range of near-neutral conditions, and the increase in Λ/l_b with increasing $-\zeta$ is relatively small. In contrast, ASL measurements span much greater ranges of ζ, and report that Λ/l_b decreases significantly. Therefore, the discrepancy may be just a local deviation from a larger-scale trend. Third, the discrepancy may be due to differences in definitions used between the DNS and ASL studies. Because of the low Reynolds number of the DNS, characteristic features of atmospheric spectra may be underdeveloped or absent in the DNS (e.g. the inertial range $k^{-5/3}$ region). The k^{-1} region fit to the DNS spectra should be interpreted as an 'effective' k^{-1} region that serves to include first-order effects of all large eddies in our analysis (Figure 8). Furthermore, the presence of a hard upper lid in our simulation – corresponding to a free-troposphere with infinite stability – is an idealization that may also contribute to differences between large-eddy length-scales estimated from the DNS and ASL measurements. Hence, DNS-observed Λ/l_b is not directly comparable with ASL measurements. In fact, close examination of Figure 6 reveals that the $\sim k^{-1}$ region ($0.03 \leq f \leq 0.4$) in the F_{bb} spectrum decreases with increasing $-\zeta$, consistent with previous experimental studies. It appears that, while the DNS k^{-1} region is decreasing with increasing $-\zeta$, as expected, even lower frequency contributions are increasing, causing the estimated Λ to increase.

6.3. *Implications for mixing-length models*

A key result is that single mixing-length models, which parametrize turbulence based on a master length-scale, appear to be insufficient for capturing dissimilarity in heat and momentum transport. A model based on a single length-scale implies the relevant compensated spectra (i.e. pre-multiplied with k) have distinct maxima. Even spectral models, which admit contributions from many different length-scales, may still assume the presence of a peak in the spectra (e.g. Claussen, 1985). Spectral peaks have also been used as a summary statistic in describing

field experiment data (e.g. Kaimal and Finnigan, 1994). However, the presence of a k^{-1} region in the temperature variance spectrum means we should not expect to find a distinct peak in the kF_{bb} compensated spectrum. Mixing-length models based on a 'master length-scale' are still widely used in both the atmospheric science (e.g. Mellor and Yamada, 1982; Janjić, 1990; Nakanishi, 2001) and fluid mechanics (e.g. Antonia and Kim, 1991; Scagliarini *et al.*, 2015) literature. The results from this analysis suggest that, while one length-scale is insufficient to capture heat and momentum transport dissimilarity, a relatively small number (possibly even two) may suffice, when incorporated into a spectral framework. These length-scales are not determined from spectral peaks but can be inferred from wavenumbers at which crossovers from one spectral scaling regime to another occur.

6.4. Does turbulent heat transport obey MOST?

These results also suggest that surface layer temperature/buoyancy transport is not strictly Monin – Obukhov similar for mildly unstable and near-neutral conditions (McNaughton and Brunet, 2002; van de Boer *et al.*, 2014), contrary to textbook knowledge (Kaimal and Finnigan, 1994). This is because ϕ_h is also a function of Λ, rather than just local length-scales. While it is known that the velocities u and v are not MO-similar, there is still substantial disagreement in the literature on the status of b. Some more recent field experiments suggest b is not MO-similar (McNaughton and Brunet, 2002). On the other hand, both LES (Khanna and Brasseur, 1997; Maronga and Reuder, 2017) and other recent field studies (Högström, 1989; de Bruin *et al.*, 1993; Choi *et al.*, 2004; Li and Bou-Zeid, 2011) suggest it is.

However, the LES studies are vulnerable to artifacts due to the SGS filter and to parametrizations near the wall, making it difficult to draw firm conclusions from these results. In arguing that b obeys MOST, the relevant field studies show that the correlations R_{uw} and R_{wT} can be modelled reasonably with empirical functions that are solely functions of ζ, and some calibration parameters. Our DNS exhibits a similar relation between R_{uw}, R_{wT} and ζ (not shown, but consistent with, e.g., Figure 6 of Li and Bou-Zeid, 2011). They argue that this is evidence for MO-similarity of heat and momentum transport. However, since our DNS agrees with these results, yet our analysis (Figure 10) clearly demonstrates that heat transport need not be MO-similar, there appears to be a contradiction. We resolve this contradiction by noting that dependence on larger length-scales, such as the height of the ABL, may well be hidden in the calibration parameters of the empirical functions fit to the data in previous field studies. Indeed, the Λ-dependence in Eq. (22) enters through a term that is relatively insensitive to variations in ζ:

$$\left\{1+\frac{2}{5}\log\left(\frac{\Lambda(\zeta)}{l_b(\zeta)}\right)\right\}^{-1},$$

where Λ and l_b are dependent on ζ. Therefore, it is possible that, while the calibration parameters do not vary significantly with ζ, they still encode an important dependence on Λ. This result demonstrates the value of a DNS study, where theories can be tested using a single, internally consistent set of results.

Previous LES (Khanna and Brasseur, 1997; Maronga and Reuder, 2017) and field (Johansson *et al.*, 2001) studies show that the relation between ϕ_m and ζ displays more scatter compared to the relation between ϕ_h and ζ. This result is not inconsistent with our study. The relation between ϕ_w and ζ displays more scatter compared to the relation between ϕ_b and ζ (Khanna and Brasseur, 1997; Johansson *et al.*, 2001; Maronga and Reuder, 2017). Our spectral model for ϕ_m is a function of ϕ_w^3; our model for ϕ_h is a function of $\phi_w\phi_b^2$. Therefore, our model predicts that $\phi_m\,(z/L)$ should display more scatter than $\phi_h\,(z/L)$, solely because $\phi_w\,(z/L)$ displays more scatter than $\phi_b\,(z/L)$. The reasons for differences in scatter between $\phi_w\,(z/L)$ and $\phi_b\,(z/L)$ remain to be determined, and may include contributions from large eddies. Our study shows that, given ϕ_w and ϕ_b, large eddies play a significant role in determining the shape of ϕ_h for the mildly unstable conditions and idealized ABL considered in this study.

6.5. Limitations

Our study is subject to various limitations, which we discuss in more detail here. First, as previously noted, the DNS is for a relatively low Reynolds number. This is in contrast to the high Reynolds number ASL, where the spectrum of turbulence spans six to seven decades, and the separation between Λ and the Kolmogorov microscale spans five to six decades. DNS spectra lack developed inertial subranges, and Kolmogorov inertial subrange scaling theory applies to a very small range of scales. It also means that results from this analysis (for instance, the scaling of l_w, l_b and Λ) are still dependent on the Reynolds number. For this reason, we refrain from proposing scaling laws for these quantities in the ASL. However, the normalized statistics are consistent with ASL measurements (Figure 5), as are the low-wavenumber components of the spectra (Figure 6), which are more relevant to heat and momentum transport. The DNS can offer a useful new perspective on low-frequency contributions to ϕ_m and ϕ_h. Furthermore, a separate analysis based on field measurements – and independent of the DNS – is consistent with the results of the DNS (Figure 3).

Second, like many other studies, the geometry is highly idealized compared to the ASL. The bottom boundary is smooth, so surface roughness is neglected. The top boundary is impermeable and not heated or cooled, so entrainment at the top of the ABL is also neglected. The finite vertical and horizontal lengths of the domain may also alter the flow statistics (Metzger *et al.*, 2007; Monty *et al.*, 2009). This configuration can be thought of as a quasi-stationary ABL over a smooth air – water interface with strong free-troposphere stability.

Third, the range of ζ considered is quite small. Our analysis is restricted to the constant-flux layer, which is small for low Reynolds numbers. Nonetheless, while there are many studies of neutral wall-bounded turbulence ($\zeta = 0$), and others of free convection ($\zeta \to -\infty$), our results span a mildly unstable set of conditions representing the transition between neutral and free-convective regimes that have received relatively little attention from DNS studies. Moreover, for the range of ζ considered here, the integral length-scale of vertical velocity variance (I_w) grows rapidly relative to the integral length-scale of buoyancy variance (I_b), suggesting this range is particularly significant in the onset of buoyancy effects on the flow.

Fourth, the model spectra used in this study are highly idealized, and their fit with DNS spectra is not always perfect (Figure 8). We have deliberately chosen functional forms with heritage in the literature (Katul *et al.*, 2013; Li *et al.*, 2015b; McColl *et al.*, 2016) that capture crossovers between different scaling regimes, but also keep the analysis tractable. Many corrections could be made to the idealized forms used here: for instance, an exponential correction could be added at high wavenumbers to account for viscous truncation of the inertial range at low Reynolds number. However, adding complexity sacrifices analytical tractability and clouds interpretation. Hence, we work with an analytically tractable, maximum-simplicity model which matches key features of the observed spectra to first order. We have also chosen forms that will easily generalize to high Reynolds number ASL conditions, at the expense of a perfect fit with the DNS spectra. For instance, while the low Reynolds number DNS spectra do not feature a prominent inertial subrange, we base our idealized spectra around this characteristic feature of high Reynolds number turbulence. The k^{-1} region is treated in this study as a simple, bulk parametrization of all large-scale motions. As new information on low-frequency contributions to spectra are revealed in future, they may be readily incorporated into this framework.

7. Conclusions

This study investigates the role of large eddies in the dissimilar turbulent transport of heat and momentum in the ASL. It is difficult to cleanly measure low-frequency contributions to turbulent transport in the ASL due to non-stationarity and potential contributions from surface roughness, entrainment and canopy effects. A DNS of an idealized, mildly unstable ASL is performed, allowing the role of large eddies in the breakdown of the Reynolds analogy to be identified, independent of other mechanisms. While the Reynolds number is low ($Re_\tau = 687$), this is among the highest Reynolds number DNS of a heated, sheared wall-bounded flow yet performed. Despite the low Reynolds number, DNS estimates of MOST statistics ϕ_b, ϕ_m and ϕ_h are consistent with field measurements (DNS-estimated ϕ_w is at the low end of field experiment measurements). The DNS-estimated turbulent spectra lack a developed inertial range, as expected for such low Reynolds numbers, but remain consistent with low-frequency components of F_{ww} and F_{bb} reported from field experiments. In particular, the DNS kF_{bb} compensated spectra exhibit broad peaks that are consistent with a k^{-1} region, observed in several field studies. Consistent with these studies, the k^{-1} region shrinks as instability increases. Overall, these results suggest that DNS can provide a new platform for analyzing ASL theories, particularly the role of low-frequency spectral components, perhaps corresponding to large-scale coherent structures. In particular, they demonstrate that the breakdown of the Reynolds analogy in the unstable ASL is not necessarily a result of factors such as surface roughness, canopy effects or entrainment, which are not included in the DNS (although these factors may contribute in the ASL).

Models for ϕ_m and ϕ_h are derived using theory, observations and the DNS. The derived models describe the partitioning of kinetic (ϕ_w, F_{ww}) and potential energy (ϕ_b, F_{bb}) between the transport of momentum (ϕ_m) and heat (ϕ_h). A spectral model based on a single length-scale is able to reproduce the DNS-observed ϕ_m, consistent with MOST. In contrast, modelling ϕ_h with a single length-scale results in a substantially biased estimate. We show that introducing a k^{-1} region in the parametrized F_{bb} spectrum, which requires the addition of a larger length-scale Λ, removes the model bias. These results are consistent with sensitivity analyses based on field measurements that are independent of the DNS. The key role of Λ in determining the shape of ϕ_h suggests turbulent transport of heat in the ASL is not MO-similar. We reconcile this result with previous field studies that argue heat transport is MO-similar, by noting that any dependence on larger length-scales could be hidden in the calibration constants of empirical functions linking ϕ_h and ζ.

These results suggest widely used single-mixing-length models may be insufficient for characterizing dissimilar transport of heat and momentum. However, there is potential for parsimoniously modelling crucial low-frequency contributions to turbulent heat transport by using an idealized spectral framework, perhaps parametrized with as few as two length-scales. As advances in computing make higher Reynolds number DNS feasible, low-frequency spectral components can be parametrized in more detail and readily included in this framework. Developing scaling relations for parametrized length-scales (and their (in)sensitivity to Reynolds number) will be a key future research task. Future studies are also needed to characterize turbulent heat transport beyond the narrow range of ζ considered in this study.

Acknowledgements

KAM acknowledges funding from the National Science Foundation (NSF) Graduate Research Fellowship Program. GGK acknowledges support from the NSF (NSF-EAR-1344703) and the US Department of Energy through the Office of Biological and Environmental Research Terrestrial Carbon Processes program (DE-SC0006967 and DE-SC0011461). PG acknowledges funding from the NSF CAREER program (NSF-EAR-1552304).

Appendix

Sensitivity to 'constant flux' and equilibrated budget assumptions

Corrections are derived here to account for violations of assumptions used in deriving the original models for ϕ_m and ϕ_h. Replace Eqs (2), (3), (11) and (13) with

$$\overline{u'w'} = -A_m u_*^2, \tag{A1}$$

$$\overline{w'b'} = A_h u_* b_*, \tag{A2}$$

$$\epsilon = \frac{\left(-\overline{u'w'}\right)^2}{k_v u_* z}\left\{\phi_m\left(\frac{z}{L}\right) - \frac{z}{L}\right\} + B_m, \tag{A3}$$

$$N_b = \frac{A_h^2 b_*^2 u_*}{k_v z}\phi_h + B_h, \tag{A4}$$

respectively. Here, A_m and A_h are corrections to the 'constant-flux' layer assumption. B_m and B_h are corrections to the assumptions of equilibrated TKE and $\overline{b'^2}$ budgets, respectively. Repeating the previous derivations using these new relations, we obtain new expressions for the mixing-length models:

$$\phi_m\left(\frac{z}{L}\right) = \frac{z}{L} + \frac{2^{5/2}\pi}{(5C_K)^{3/2}}\frac{1}{A_m^2}\left(\frac{k_v z}{l_w}\right)\phi_w^3 - \frac{k_v z B_m}{A_m^2 u_*^3}, \tag{A5}$$

$$\phi_h\left(\frac{z}{L}\right) = \left(\frac{2^{5/2}\pi}{5^{3/2}C_T C_K^{1/2}}\right)\frac{1}{A_h^2}\left(\frac{k_v z}{l_w^{1/3} l_b^{2/3}}\right)\phi_w\phi_b^2 - \frac{k_v z B_h}{A_h^2 u_* b_*^2}. \tag{A6}$$

We also obtain a new expression for the new model:

$$\phi_h\left(\frac{z}{L}\right) = \left(\frac{2^{5/2}\pi}{5^{3/2}C_T C_K^{1/2}}\right)\frac{1}{A_h^2}\left(\frac{1}{1+\frac{2}{5}\log\left(\frac{\Lambda}{l_b}\right)}\right)\left(\frac{k_v z}{l_w^{1/3} l_b^{2/3}}\right)\phi_w\phi_b^2 - \frac{k_v z B_h}{A_h^2 u_* b_*^2}. \tag{A7}$$

The constants A_m, A_h, B_m and B_h are estimated from the DNS, and used to correct for violations of these assumptions.

References

Abe H, Kawamura H, Matsuo Y. 2004. Surface heat-flux fluctuations in a turbulent channel flow up to $Re = 1020$ with $Pr = 0.025$ and 0.71. *Int. J. Heat Fluid Flow* **25**: 404–419. https://doi.org/10.1016/j.ijheatfluidflow.2004.02.010.

Adrian RJ. 2007. Hairpin vortex organization in wall turbulence. *Phys. Fluids* **19**: 041301. https://doi.org/10.1063/1.2717527.

Ansorge C, Mellado JP. 2014. Global intermittency and collapsing turbulence in the stratified planetary boundary layer. *Boundary-Layer Meteorol.* **153**: 89–116. https://doi.org/10.1007/s10546-014-9941-3.

Antonia RA, Kim J. 1991. Reynolds shear stress and heat flux calculations in a fully developed turbulent duct flow. *Int. J. Heat Mass Transfer* **34**: 2013–2018. https://doi.org/10.1016/0017-9310(91)90212-W.

van de Boer A, Moene AF, Graf A, Schüttemeyer D, Simmer C. 2014. Detection of entrainment influences on surface-layer measurements and extension of Monin – Obukhov similarity theory. *Boundary-Layer Meteorol.* **152**: 19–44. https://doi.org/10.1007/s10546-014-9920-8.

Bosveld FC, Baas P, Steeneveld GJ, Holtslag AAM, Angevine WM, Bazile E, Bruijn EIFd, Deacu D, Edwards JM, Ek M, Larson VE, Pleim JE, Raschendorfer M, Svensson G. 2014. The third GABLS intercomparison case for evaluation studies of boundary-layer models. Part B: Results and process understanding. *Boundary-Layer Meteorol.* **152**: 157–187. https://doi.org/10.1007/s10546-014-9919-1.

Bradley EF, Antonia RA. 1979. Structure parameters in the atmospheric surface layer. *Q. J. R. Meteorol. Soc.* **105**: 695–705. https://doi.org/10.1002/qj.49710544513.

Brasseur JG, Wei T. 2010. Designing large-eddy simulation of the turbulent boundary layer to capture law-of-the-wall scaling. *Phys. Fluids* **22**: 021303. https://doi.org/10.1063/1.3319073.

de Bruin HAR, Kohsiek W, van den Hurk BJJM. 1993. A verification of some methods to determine the fluxes of momentum, sensible heat, and water vapour using standard deviation and structure parameter of scalar meteorological quantities. *Boundary-Layer Meteorol.* **63**: 231–257. https://doi.org/10.1007/BF00710461.

Brutsaert W. 1982. *Evaporation into the Atmosphere*. Springer: Dordrecht, Netherlands.

Busch NE, Panofsky HA. 1968. Recent spectra of atmospheric turbulence. *Q. J. R. Meteorol. Soc.* **94**: 132–148. https://doi.org/10.1002/qj.49709440003.

Businger JA. 1973. A note on free convection. *Boundary-Layer Meteorol.* **4**: 323–326. https://doi.org/10.1007/BF02265241.

Businger JA, Wyngaard JC, Izumi Y, Bradley EF. 1971. Flux-profile relationships in the atmospheric surface layer. *J. Atmos. Sci.* **28**: 181–189. doi:10.1175/1520-0469(1971)028⟨0181:fprita⟩2.0.CO;2.

Choi T, Hong J, Kim J, Lee H, Asanuma J, Ishikawa H, Tsukamoto O, Zhiqiu G, Ma Y, Ueno K, Wang J, Koike T, Yasunari T. 2004. Turbulent exchange of heat, water vapor, and momentum over a Tibetan prairie by eddy covariance and flux variance measurements. *J. Geophys. Res. Atmos.* **109**: D21106. https://doi.org/10.1029/2004JD004767.

Chung D, Matheou G. 2012. Direct numerical simulation of stationary homogeneous stratified sheared turbulence. *J. Fluid Mech.* **696**: 434–467. https://doi.org/10.1017/jfm.2012.59.

Claussen M. 1985a. Estimation of the monin-obukhov similarity functions from a spectral model. *Boundary-Layer Meteorol.* **33**: 233–243.

Claussen M. 1985b. A model of turbulence spectra in the atmospheric surface layer. *Boundary-Layer Meteorol.* **33**: 151–172. https://doi.org/10.1007/BF00123388.

Dong YH, Lu XY. 2005. Direct numerical simulation of stably and unstably stratified turbulent open channel flows. *Acta Mech.* **177**: 115–136. https://doi.org/10.1007/s00707-005-0229-z.

Dyer AJ, Hicks BB. 1970. Flux-gradient relationships in the constant flux layer. *Q. J. R. Meteorol. Soc.* **96**: 715–721. https://doi.org/10.1002/qj.49709641012.

Garai A, Kleissl J, Sarkar S. 2014. Flow and heat transfer in convectively unstable turbulent channel flow with solid-wall heat conduction. *J. Fluid Mech.* **757**: 57–81. https://doi.org/10.1017/jfm.2014.479.

Garcia JR, Mellado JP. 2014. The two-layer structure of the entrainment zone in the convective boundary layer. *J. Atmos. Sci.* **71**: 1935–1955. https://doi.org/10.1175/JAS-D-13-0148.1.

Gioia G, Guttenberg N, Goldenfeld N, Chakraborty P. 2010. Spectral theory of the turbulent mean-velocity profile. *Phys. Rev. Lett.* **105**: 184501. https://doi.org/10.1103/PhysRevLett.105.184501.

Haugen DA, Kaimal JC, Bradley EF. 1971. An experimental study of Reynolds stress and heat flux in the atmospheric surface layer. *Q. J. R. Meteorol. Soc.* **97**: 168–180. https://doi.org/10.1002/qj.49709741204.

He P, Basu S. 2015. Development of similarity relationships for energy dissipation rate and temperature structure parameter in stably stratified flows: A direct numerical simulation approach. *Environ. Fluid Mech.* **16**: 373–399. https://doi.org/10.1007/s10652-015-9427-y.

Head MR, Bandyopadhyay P. 1981. New aspects of turbulent boundary-layer structure. *J. Fluid Mech.* **107**: 297338. https://doi.org/10.1017/S0022112081001791.

van Heerwaarden CC, Mellado JP. 2016. Growth and decay of a convective boundary layer over a surface with a constant temperature. *J. Atmos. Sci.* **73**: 2165–2177. https://doi.org/10.1175/JAS-D-15-0315.1.

van Heerwaarden CC, Mellado JP, De Lozar A. 2014. Scaling laws for the heterogeneously heated free convective boundary layer. *J. Atmos. Sci.* **71**: 3975–4000. https://doi.org/10.1175/JAS-D-13-0383.1.

van Heerwaarden CC, van Stratum BJH, Heus T, Gibbs JA, Fedorovich E, Mellado JP. 2017. MicroHH 1.0: A computational fluid dynamics code for direct numerical simulation and large-eddy simulation of atmospheric boundary layer flows. *Geosci. Model Dev. Discuss.* in review. https://doi.org/10.5194/gmd-2017-41.

Högström U. 1988. Non-dimensional wind and temperature profiles in the atmospheric surface layer: A re-evaluation. *Boundary-Layer Meteorol.* **42**: 55–78. https://doi.org/10.1007/BF00119875.

Högström U. 1989. Analysis of turbulence structure in the surface layer with a modified similarity formulation for near neutral conditions. *J. Atmos. Sci.* **47**: 1949–1972. https://doi.org/10.1175/1520-0469(1990)047$⟨$1949:aotsit$⟩$2.0.CO;2.

Högström U, Hunt JCR, Smedman AS. 2002. Theory and measurements for turbulence spectra and variances in the atmospheric neutral surface layer. *Boundary-Layer Meteorol.* **103**: 101–124. https://doi.org/10.1023/A:1014579828712.

Hommema SE, Adrian RJ. 2003. Packet structure of surface eddies in the atmospheric boundary layer. *Boundary-Layer Meteorol.* **106**: 147–170. https://doi.org/10.1023/A:1020868132429.

Iida O, Kasagi N. 1997. Direct numerical simulation of unstably stratified turbulent channel flow. *J. Heat Transfer* **119**: 53–61. https://doi.org/10.1115/1.2824100.

Janjić ZI. 1990. The step-mountain coordinate: Physical package. *Mon. Weather Rev.* **118**: 1429–1443. https://doi.org/10.1175/1520-0493(1990)118$⟨$1429:tsmcpp$⟩$2.0.CO;2.

Johansson C, Smedman AS, Högström U, Brasseur JG, Khanna S. 2001. Critical test of the validity of Monin – Obukhov similarity during convective conditions. *J. Atmos. Sci.* **58**: 1549–1566. https://doi.org/10.1175/1520-0469(2001)058⟨1549:ctotvo⟩2.0.CO;2.

Kader BA, Yaglom AM. 1990. Mean fields and fluctuation moments in unstably stratified turbulent boundary layers. *J. Fluid Mech.* **212**: 637–662.

Kader BA, Yaglom AM. 1991. Spectra and correlation functions of surface layer atmospheric turbulence in unstable thermal stratification. In *Turbulence and Coherent Structures*, Metais O, Lesieur M. (eds.), *Fluid Mechanics and Its Applications*, **2**: 387–412. Springer: Dordrecht, Netherlands.

Kaimal JC, Finnigan JJ. 1994. *Atmospheric Boundary-Layer Flows: Their Structure and Measurement*. Oxford University Press: New York, NY.

Kaimal JC, Wyngaard JC, Izumi Y, Coté OR. 1972. Spectral characteristics of surface-layer turbulence. *Q. J. R. Meteorol. Soc.* **98**: 563–589. https://doi.org/10.1002/qj.49709841707.

Katul GG, Chu CR, Parlange MB, Albertson JD, Ortenburger TA. 1995. Low-wavenumber spectral characteristics of velocity and temperature in the atmospheric surface layer. *J. Geophys. Res. Atmos.* **100**: 14243–14255. https://doi.org/10.1029/94JD02616.

Katul GG, Hsieh CI, Kuhn G, Ellsworth D, Nie D. 1997. Turbulent eddy motion at the forest – atmosphere interface. *J. Geophys. Res. Atmos.* **102**: 13409–13421. https://doi.org/10.1029/97JD00777.

Katul GG, Konings AG, Porporato A. 2011. Mean velocity profile in a sheared and thermally stratified atmospheric boundary layer. *Phys. Rev. Lett.* **107**: 268502. https://doi.org/10.1103/PhysRevLett.107.268502.

Katul GG, Li D, Chamecki M, Bou-Zeid E. 2013. Mean scalar concentration profile in a sheared and thermally stratified atmospheric surface layer. *Phys. Rev. E* **87**: 023004. https://doi.org/10.1103/PhysRevE.87.023004.

Katul GG, Porporato A, Shah S, Bou-Zeid E. 2014. Two phenomenological constants explain similarity laws in stably stratified turbulence. *Phys. Rev. E* **89**: 023007. https://doi.org/10.1103/PhysRevE.89.023007.

Katul GG, Li D, Liu H, Assouline S. 2016. Deviations from unity of the ratio of the turbulent Schmidt to Prandtl numbers in stratified atmospheric flows over water surfaces. *Phys. Rev. Fluids* **1**: 034401. https://doi.org/10.1103/PhysRevFluids.1.034401.

Khanna S, Brasseur JG. 1997. Analysis of Monin – Obukhov similarity from large-eddy simulation. *J. Fluid Mech.* **345**: 251–286. https://doi.org/10.1017/S0022112097006277.

Kolmogorov A. 1941. The local structure of turbulence in incompressible viscous fluids for very large Reynolds numbers. *Dokl. Akad. Nauk. SSSR* **30**: 299–303.

Lee M, Moser RD. 2015. Direct numerical simulation of turbulent channel flow up to $re_\tau \approx 5200$. *J. Fluid Mech.* **774**: 395–415.

Li D, Bou-Zeid E. 2011. Coherent structures and the dissimilarity of turbulent transport of momentum and scalars in the unstable atmospheric surface layer. *Boundary-Layer Meteorol.* **140**: 243–262. https://doi.org/10.1007/s10546-011-9613-5.

Li D, Katul GG, Bou-Zeid E. 2012. Mean velocity and temperature profiles in a sheared diabatic turbulent boundary layer. *Phys. Fluids* **24**: 105105. https://doi.org/10.1063/1.4757660.

Li D, Katul GG, Bou-Zeid E. 2015a. Turbulent energy spectra and cospectra of momentum and heat fluxes in the stable atmospheric surface layer. *Boundary-Layer Meteorol.* **157**: 1–21. https://doi.org/10.1007/s10546-015-0048-2.

Li D, Katul GG, Zilitinkevich SS. 2015b. Revisiting the turbulent Prandtl number in an idealized atmospheric surface layer. *J. Atmos. Sci.* **72**: 2394–2410. https://doi.org/10.1175/JAS-D-14-0335.1.

Li D, Salesky ST, Banerjee T. 2016a. Connections between the Ozmidov scale and mean velocity profile in stably stratified atmospheric surface layers. *J. Fluid Mech.* **797**: R3. https://doi.org/10.1017/jfm.2016.311.

Li D, Katul GG, Gentine P. 2016b. The k^{-1} scaling of air temperature spectra in atmospheric surface layer flows. *Q. J. R. Meteorol. Soc.* **142**: 496–505. https://doi.org/10.1002/qj.2668.

Lynch RA, Bradley EF. 1974. Shearing stress meter. *J. Appl. Meteorol.* **13**: 588–591. https://doi.org/10.1175/1520-0450(1974)013⟨0588:ssm⟩2.0.CO;2.

McBean G. 1970. 'The turbulent transfer mechanisms in the atmospheric surface layer', PhD thesis. University of British Columbia: Canada.

McColl KA, Katul GG, Gentine P, Entekhabi D. 2016. Mean-velocity profile of smooth channel flow explained by a cospectral budget model with wall-blockage. *Phys. Fluids* **28**: 035107. https://doi.org/10.1063/1.4943599.

McNaughton KG, Brunet Y. 2002. Townsend's hypothesis, coherent structures and Monin Obukhov similarity. *Boundary-Layer Meteorol.* **102**: 161–175.

Maronga B, Reuder J. 2017. On the formulation and universality of Monin – Obukhov similarity functions for mean gradients and standard deviations in the unstable surface layer: Results from surface-layer-resolving large-eddy simulations. *J. Atmos. Sci.* **74**: 989–1010. https://doi.org/10.1175/JAS-D-16-0186.1.

Mellado JP, Heerwaarden CCv, Garcia JR. 2015. Near-surface effects of free atmosphere stratification in free xonvection. *Boundary-Layer Meteorol.* **159**: 69–95. https://doi.org/10.1007/s10546-015-0105-x.

Mellor GL. 1973. Analytic prediction of the properties of stratified planetary surface layers. *J. Atmos. Sci.* **30**: 1061–1069. https://doi.org/10.1175/1520-0469(1973)030⟨1061:apotpo⟩2.0.CO;2.

Mellor GL, Yamada T. 1982. Development of a turbulence closure model for geophysical fluid problems. *Rev. Geophys.* **20**: 851–875. https://doi.org/10.1029/RG020i004p00851.

Metzger M, McKeon BJ, Holmes H. 2007. The near-neutral atmospheric surface layer: Turbulence and non-stationarity. *Phil. Trans. R. Soc. London, Ser. A* **365**: 859–876. https://doi.org/10.1098/rsta.2006.1946.

Miyake M, Stewart RW, Burling RW. 1970. Spectra and cospectra of turbulence over water. *Q. J. R. Meteorol. Soc.* **96**: 138–143. https://doi.org/10.1002/qj.49709640714.

Monin A, Obukhov A. 1954. Basic laws of turbulent mixing in the surface layer of the atmosphere. *Tr. Geofiz. Inst.* **24**: 163–187.

Monty JP, Hutchins N, Ng HCH, Marusic I, Chong MS. 2009. A comparison of turbulent pipe, channel and boundary-layer flows. *J. Fluid Mech.* **632**: 431–442. https://doi.org/10.1017/S0022112009007423.

Morinishi Y, Lund TS, Vasilyev OV, Moin P. 1998. Fully conservative higher-order finite difference schemes for incompressible flow. *J. Comput. Phys.* **143**: 90–124. https://doi.org/10.1006/jcph.1998.5962.

Nakanishi M. 2001. Improvement of the Mellor – Yamada turbulence closure model based on large-eddy simulation data. *Boundary-Layer Meteorol.* **99**: 349–378. https://doi.org/10.1023/A:1018915827400.

Patton EG, Sullivan PP, Shaw RH, Finnigan JJ, Weil JC. 2015. Atmospheric stability influences on coupled boundary-layer and canopy turbulence. *J. Atmos. Sci.* **73**: 1621–1647. https://doi.org/10.1175/JAS-D-15-0068.1.

Pena A, Gryning SE, Mann J. 2010. On the length-scale of the wind profile. *Q. J. R. Meteorol. Soc.* **136**: 2119–2131. https://doi.org/10.1002/qj.714653.

Perry AE, Chong MS. 1982. On the mechanism of wall turbulence. *J. Fluid Mech.* **119**: 173–217. https://doi.org/10.1017/S0022112082001311.

Phelps GT, Pond S. 1971. Spectra of the temperature and humidity fluctuations and of the fluxes of moisture and sensible heat in the marine boundary layer. *J. Atmos. Sci.* **28**: 918–928. https://doi.org/10.1175/1520-0469(1971)028⟨0918:sottah⟩2.0.CO;2.

Prandtl L. 1925. Bericht uber Untersuchungen zur ausgebildeten Turbulenz. *Z. Angew. Math. Mech.* **5**: 136–139.

Salesky ST, Katul GG, Chamecki M. 2013. Buoyancy effects on the integral length-scales and mean velocity profile in atmospheric surface layer flows. *Phys. Fluids* **25**: 105101. https://doi.org/10.1063/1.4823747.

Scagliarini A, Einarsson H, Gylfason Á, Toschi F. 2015. Law of the wall in an unstably stratified turbulent channel flow. *J. Fluid Mech.* **781**: R5. https://doi.org/10.1017/jfm.2015.498.

Shin HH, Hong SY. 2011. Intercomparison of planetary boundary-layer parametrizations in the WRF model for a single day from CASES-99. *Boundary-Layer Meteorol.* **139**: 261–281. https://doi.org/10.1007/s10546-010-9583-z.

Stevens B. 2000. Quasi-steady analysis of a PBL model with an eddy-diffusivity profile and nonlocal fluxes. *Mon. Weather Rev.* **128**: 824–836. https://doi.org/10.1175/1520-0493(2000)128⟨0824:qsaoap⟩2.0.CO;2.

Stull RB. 1988. *An Introduction to Boundary-Layer Meteorology*. Kluwer: Dordrecht, Netherlands.

Sullivan PP, Patton EG. 2011. The effect of mesh resolution on convective boundary layer statistics and structures generated by large-eddy simulation. *J. Atmos. Sci.* **68**: 2395–2415. doi:10.1175/JAS-D-10-05010.1.

Taylor GI. 1938. The spectrum of turbulence. *Proc. R. Soc. London, Ser. A* **164**: 476–490. https://doi.org/10.1098/rspa.1938.0032.

Therry G, Lacarrere P. 1983. Improving the Eddy Kinetic Energy model for planetary boundary layer description. *Boundary-Layer Meteorol.* **25**: 63–88. https://doi.org/10.1007/BF00122098.

Townsend AA. 1980. *The Structure of Turbulent Shear Flow*. Cambridge University Press: Cambridge, UK.

Vercauteren N, Bou-Zeid E, Parlange MB, Lemmin U, Huwald H, Selker J, Meneveau C. 2008. Subgrid-scale dynamics of water vapour, heat, and momentum over a lake. *Boundary-Layer Meteorol.* **128**: 205–228. https://doi.org/10.1007/s10546-008-9287-9.

van de Wiel BJH, Moene AF, Ronde WHD, Jonker HJJ. 2008. Local similarity in the stable boundary layer and mixing-length approaches: Consistency of concepts. *Boundary-Layer Meteorol.* **128**: 103–116. doi:10.1007/s10546-008-9277-y.

Wyngaard JC, Coté OR, Izumi Y. 1971. Local free convection, similarity, and the budgets of shear stress and heat flux. *J. Atmos. Sci.* **28**: 1171–1182. doi:10.1175/1520-0469(1971)028⟨1171:lfcsat⟩2.0.CO;2.

Zhang H, Trias FX, Gorobets A, Tan Y, Oliva A. 2015. Direct numerical simulation of a fully developed turbulent square duct flow up to. *Int. J. Heat Fluid Flow* **54**: 258–267. https://doi.org/10.1016/j.ijheatfluidflow.2015.06.003.

Zhu Z, Yang H, Chen T. 2010. Numerical study of turbulent heat and fluid flow in a straight square duct at higher Reynolds numbers. *Int. J. Heat Mass Transfer* **53**: 356–364. https://doi.org/10.1016/j.ijheatmasstransfer.2009.09.021.

Zilitinkevich SS, Hunt JCR, Esau IN, Grachev AA, Lalas DP, Akylas E, Tombrou M, Fairall CW, Fernando HJS, Baklanov AA, Joffre SM. 2006. The influence of large convective eddies on the surface-layer turbulence. *Q. J. R. Meteorol. Soc.* **132**: 1423–1456. https://doi.org/10.1256/qj.05.79.

Zonta F, Soldati A. 2013. Effect of temperature dependent fluid properties on heat transfer in turbulent mixed convection. *J. Heat Transfer* **136**: 022501. https://doi.org/10.1115/1.4025135.

